

21 **Abstract**

22 Understanding the uptake of a drug by diseased tissue, and the drug's subsequent
23 spatiotemporal distribution, are central factors in the development of effective targeted
24 therapies. However, the interaction between the pathophysiology of diseased tissue and
25 individual therapeutic agents can be complex, and can vary across tissue types and across
26 subjects. Here, we show that the combination of mathematical modelling, of high-resolution
27 optical imaging of intact and optically cleared tumour tissue from animal models, and of in
28 vivo imaging of vascular perfusion predicts the heterogeneous uptake, by large tissue
29 samples, of specific therapeutic agents, as well as their spatiotemporal distribution. In
30 particular, by using murine models of colorectal cancer and glioma, we report and validate
31 predictions of steady-state blood flow and intravascular and interstitial fluid pressure in
32 tumours, of the spatially heterogeneous uptake of chelated gadolinium by tumours, and of
33 the effect of a vascular disrupting agent on tumour vasculature.

34 Introduction

35 Mathematical modelling of biological tissue is increasingly used to better understand
36 complex biological phenomena, such as the development of disease.¹ This developing
37 paradigm of computational experimentation can enable subtle interventions to be
38 performed in a manner that would be challenging or impossible in a conventional
39 experimental setting. In this study we present a framework for performing realistic
40 computational experiments that naturally incorporates the variability and heterogeneity
41 found between biological samples. It allows large tissue samples to be imaged and treated
42 as living specimens, by combining cutting-edge optical and *in vivo* imaging techniques with
43 mathematical modelling. We have named our framework REANIMATE (REalistic Numerical
44 Image-based Modelling of biologicaI Tissue substratEs) (see **Figure 1** for an overview
45 diagram).

46 Optical imaging of cleared tissue can provide three-dimensional data detailing complex,
47 interacting structures (such as blood vessel networks, cell nuclei, etc.), which can be
48 explored, across entire organs,^{2,3} and at resolutions of a few microns,⁴ by using
49 fluorescently-labelled probes that bind to specific structures. Our use of large, high resolution
50 structural images in computational simulations, rather than relying on small, isolated
51 samples or synthetically-generated substrates, is a key development, and has required the
52 development of new image analysis and computational modelling approaches. Furthermore,
53 by incorporating *in vivo* imaging (in particular, magnetic resonance imaging (MRI)),
54 REANIMATE can incorporate quantitative measurements.

55 Capturing the physiological variation in complete tissue specimens is particularly useful in
56 tumors, which can be highly heterogeneous, both between tumor types, tumor deposits and
57 even within individual tumors.⁵ This results in substantial differences in, for example, drug
58 delivery, oxygenation and gene expression,⁶ with associated differences in therapeutic
59 response and resistance. Effective therapy normally requires drugs to be delivered to the
60 site of disease, at as high a concentration as possible, but avoiding significant toxicity effects
61 in healthy tissues, whilst sub-optimal exposure can limit treatment efficacy, induce
62 exposure-mediated resistance mechanisms,⁷ or even stimulate tumor growth.⁸

63 This complex physiological-pharmacological landscape requires careful analysis in order to
64 be fully understood. The numerical modelling component of REANIMATE consists of two
65 steps: first, a solution is sought from a set of coupled fluid dynamics models that describe

66 steady-state vascular and interstitial fluid transport; second, the steady-state solution (or set
67 of solutions) is used to parameterise a time-dependent model that describes the vascular
68 and interstitial uptake of exogenously administered material. This can be used, for example,
69 to model the heterogeneous pharmacokinetics of drug or imaging contrast agents, or delivery
70 of individual particles (e.g. T-cells, antibodies), and terms can be introduced to describe drug
71 targetting and metabolism.

72 For the predictions made by our, or any, computational experiments to be confidently
73 accepted, careful experimental validation must be performed. As a first evaluation, we have
74 used REANIMATE to: 1) study the spatially heterogeneous uptake of a gadolinium-based MRI
75 compound (which allowed us to compare numerical modelling solutions with ground-truth
76 *in vivo* data); and 2) investigate the effect of the vascular disrupting agent (VDA) Oxi4503 on
77 tumor vasculature. These results provided a rich, three-dimensional framework for probing
78 spatially heterogeneous tumor drug delivery and treatment response.

79 **Results**

80 *Preparation of tissue substrates for mathematical modelling*

81 We began the development of the REANIMATE framework by studying SW1222 and LS174T
82 human colorectal carcinoma tumors, implanted subcutaneously on the flank of
83 immunocompromised mice. These tumor types have been extensively studied, by our group
84 and others, with SW1222 tumors displaying greater cell differentiation, more uniform
85 vasculature and greater perfusion than LS174T tumors.⁹⁻¹⁵ Tumors of each type (n=5 of each)
86 were grown subcutaneously in mice for 10 to 14 days, and then administered fluorescently-
87 labelled lectin (AlexaFluor-647) via a tail vein, in order to fluorescently label vascular
88 structures in the tumors.² Following a circulation time of 5 minutes, tumors were resected,
89 optically cleared with benzyl-alcohol / benzyl-benzoate (BABB), and imaged, intact, with
90 optical projection tomography (OPT).¹⁶

91 Depending on the size of the tumor, our OPT images exhibited a variable background
92 autofluorescence signal, with a decrease in signal intensity towards the centre due to less
93 effective optical clearing. This was corrected by subtracting a three-dimensional Gaussian-
94 filtered copy of the data, to normalise variations in signal intensity. Blood vessels were then
95 segmented from OPT images using Frangi filtering¹⁷ and thresholding, and converted into
96 graph format with a skeletonisation algorithm. These spatial graphs consisted of nodes

97 (branch points) and vessel segments, and were typically composed of 30,000 to 200,000
98 nodes. Examples of segmented, whole-tumor blood vessel networks from example LS174T
99 and SW1222 tumors are shown in **Figure 2**.

100 We compared vessel architecture from SW1222 and LS174T tumors against previously
101 published data (obtained using a range of imaging techniques, and principally derived from
102 our own published studies), which showed that vessel architecture was preserved during
103 tissue clearing, and that our image processing algorithms accurately reproduced vessel
104 networks (see **sections 1.2 and 1.2** in the **Supplementary Information**).

105 *REANIMATE steady-state simulation in subcutaneous colorectal carcinoma xenografts*

106 Our next aim was to use whole-tumor blood vessel networks as the substrate for simulations
107 of steady-state fluid dynamics. Our mathematical model comprised of coupled intravascular
108 and interstitial compartments, with exchange mediated by vascular permeability and
109 described by Starling's Law. Blood flow and interstitial delivery were modelled using
110 Poiseuille flow and Darcy's law, respectively, and the model was optimised over the entire
111 tumor through the prescription of the pressure boundary conditions at peritumoral
112 boundary vessels. We performed our initial simulations on a set of LS174T and SW1222
113 colorectal adenocarcinoma xenografts.

114 As shown in the summary of simulated parameter values in **Supplementary Table 1**,
115 solutions to our mathematical model predicted significant differences between SW1222 and
116 LS174T tumors, in blood flow, blood velocity and vessel wall shear stress, which are
117 consistent with their known characteristics. Example spatial distributions of each of these
118 REANIMATE parameters are shown in **Figure 3**, in which vascular parameters (blood flow
119 and pressure) are displayed as colored vessel segments and interstitial parameters
120 (interstitial fluid pressure (IFP), interstitial fluid velocity (IFV) and perfusion) as overlaid color
121 fields. Results are shown for example LS174T (**Figure 3a-e**) and SW1222 tumors (**Figure 3f-j**).

122 Key to the interpretation of these results was our ability to compare them directly with
123 equivalent *in vivo* imaging data (in this case arterial spin labelling magnetic resonance
124 imaging (ASL-MRI)), which can be used to quantify perfusion, noninvasively.⁹ Perfusion is a
125 measure of the rate of delivery of fluid to biological tissue, and is dependent on blood flow,
126 vascular permeability and interstitial density, amongst other factors.¹⁸ Comparisons of ASL-
127 MRI *in vivo* measurements and REANIMATE predictions are shown in **Figures 3c** (LS174T)
128 and **3h** (SW1222), which shows a clear correspondence between the two data types.

129 Statistical analysis revealed no significant differences between predicted and measured
130 perfusion values ($p < 0.01$, Kolmogorov-Smirnov). Scatter plots of both measurements are
131 shown in **Supplementary Figures 1a and b**, which revealed a significant correlation between
132 the two measurements (LS174T, $r^2 = 0.82$, $p < 0.001$; SW1222 $r^2 = 0.89$, $p < 0.001$; Pearson
133 test). Likewise, in both *in vivo* measurements and simulations, perfusion was distributed
134 heterogeneously throughout the tumors, with markedly raised values at the periphery of
135 both types of colorectal tumor. This spatial distribution is characteristic of solid tumors,
136 particularly subcutaneous xenograft models.¹⁹ However, some regional differences were
137 also evident between simulated and ASL perfusion values, but which could have been
138 caused by errors in either value, and/or errors in the spatial registration of the two types of
139 data.

140 Both *in vivo* measurements and simulations showed that SW1222 tumors were better
141 perfused than LS174T tumors, which is again consistent with the results of previous
142 studies.²⁰ However, perfusion at the centre of SW1222 tumors was much greater than in
143 LS174T tumors, both in simulations and *in vivo* data. On average, we found that simulated
144 perfusion values in LS174T tumors matched those measured *in vivo* with MRI (0.18 ± 0.07
145 and $0.19 \pm 0.08 \text{ mL g}^{-1} \text{ min}^{-1}$) for simulated and *in vivo* measurements, respectively), whilst
146 SW1222 estimates were slightly larger, but of the same order as *in vivo* measurements (0.33
147 ± 0.18 and $0.73 \pm 0.03 \text{ mL g}^{-1} \text{ min}^{-1}$).

148 REANIMATE also predicted elevated interstitial fluid pressure in both tumor types, with
149 typical values in the range 12 to 25 mm Hg in the center of tumors, and which declined
150 towards the periphery. This, again, is consistent with the known characteristics of these
151 types of tumor, and no significant difference was measured between LS174T and SW1222
152 tumors.²¹ However, in both tumor types, IFP was not uniformly distributed, but instead
153 varied by up to 10 mm Hg within the center of individual tumors. IFP was raised at the
154 location of perfused vasculature, producing intratumoral advection effects (as can be seen in
155 the interstitial velocity images in **Figures 3e and 3j**). These results agree with previous
156 measurements of IFP and IFV from our own laboratory, in which mean IFP was measured to
157 be $16 \pm 5 \text{ mm Hg}$ in LS174T tumors and 13 ± 2 in SW1222 tumors, for a tumor volume of 0.1
158 cm^3 .²¹

159 As our optimisation procedure for the assignment of pressure boundary condition has a
160 potentially large number of solutions, we sought to determine the variability observed in
161 vascular pressure predictions across multiple simulation runs. This experiment is described

162 in the **Supplementary Information**, and from which we found that the mean standard
163 deviation of vascular pressure predictions, across simulation runs, was 0.25 mm Hg and 0.49
164 mm Hg in LS174T and SW1222 tumors, respectively. This is much smaller than the variability
165 associated with spatial heterogeneity within the tumors (8.8 and 9.2 mm Hg, respectively).

166 *REANIMATE steady-state simulation in an orthotopic murine glioma model*

167 In order to evaluate the generalisability of the REANIMATE framework, we next applied it to
168 data from orthotopic murine glioma tumors, derived from the murine GL261 cell line. At 20
169 days following the injection of glioma cells into the brain, tumors were resected from mice
170 with a section of normal cortex tissue attached. Segmented tumor and cortex vessels are
171 shown in **Figure 4a**, with brain vessels labelled in blue and tumor vessels in red.

172 As with colorectal tumors, steady-state vascular and interstitial REANIMATE fluid flow
173 solutions were generated, which are shown in **Figures 4b to 4f**. The simulations predicted
174 raised interstitial fluid pressure within the tumor (mean, 16 ± 10 mm Hg), and a mean
175 interstitial perfusion of 1.3 ± 0.5 mL min⁻¹ g⁻¹. Comparison of these simulation results with *in*
176 *vivo* measurements using ASL-MRI (shown in **Figure 4d**) revealed a good correspondence,
177 with a mean measured tumor perfusion of 1.1 ± 0.7 mL min⁻¹ g⁻¹, and equivalent spatial
178 distribution (hyperperfused periphery and central hypoperfusion). A scatter plot of the data
179 is shown in **Supplementary Figure 1c**, which revealed a significant correlation between the
180 two measurements ($r^2 = 0.91$, $p < 0.001$, Pearson test).

181 Compared with subcutaneous tumors, REANIMATE predicted orthotopic gliomas to have a
182 more uniform central IFP, which varied within a range of ± 4 mm Hg. IFV was correspondingly
183 low in the centre (< 0.01 $\mu\text{m s}^{-1}$), and high at the periphery (indeed, much higher than in
184 subcutaneous tumors (17 ± 4 $\mu\text{m s}^{-1}$)). No measurements of IFP or IFV exist in the literature
185 to compare these data against, presumably due to the technical challenges associated with
186 their measurement in deep-seated tumors.

187 In combination, these results demonstrate that mathematical modelling of fluid dynamics
188 using optical image data from cleared tumor tissue as a substrate, is both feasible and
189 provides quantitative predictions of vascular perfusion that are in keeping with experimental
190 results. Therefore our next step was to use the steady-state flow predictions to
191 parameterise a time-dependent model to simulate the delivery of exogenously-administered
192 material.

193 *REANIMATE prediction of Gd-DTPA delivery*

194 As a first evaluation, we chose to model the dynamics of chelated gadolinium (Gd-DTPA), a
195 widely used MRI contrast agent with well-studied pharmacokinetics, and directly compare
196 them with *in vivo* measurements. Gd-DTPA can be thought of as a proxy for a non-
197 metabolised therapeutic agent. Time-dependent simulations were calculated using a
198 ‘propagating front’ algorithm, that used steady-state solutions to mimic the physical delivery
199 of material, both via vascular flow and by diffusion across blood vessel wall and through the
200 interstitium.

201 To provide ground-truth data for comparison, and to generate new modelling substrates, we
202 performed *in vivo* experiments to measure the delivery of a bolus of Gd-DTPA in a set of
203 LS174T (n=5) and SW1222 (n=6) tumors, using a dynamic contrast-enhanced (DCE) MRI
204 sequence (**Figure 5**). Following these measurements, mice were culled via cervical
205 dislocation. We resected and set two tumors aside (one LS174T and one SW1222) for
206 processing within the REANIMATE framework.

207 Here, steady-state simulations were performed as described above, and were used as the
208 basis for time-dependent delivery simulations. The influence of each vessel network inlet
209 was modelled independently, and an algorithm was developed that monitored a
210 propagating front through the network. Exchange between the vascular and interstitium
211 was cast in a finite element framework, with vessel permeability (to Gd-DTPA flux) initially
212 fixed at $1 \times 10^{-6} \text{ cm s}^{-1}$.^{22,23} The interstitium was modelled as a continuum with a constant cell
213 volume fraction ($f_c = 0.8$ ²⁴). Gd-DTPA does not cross the cell membrane,²⁵ and so Gd-DTPA
214 concentration ([Gd]) was scaled by the fractional volume of the extra-cellular space, and we
215 assumed a constant diffusion through the interstitium ($D = 2.08 \times 10^{-4} \text{ mm}^2 \text{ s}^{-1}$ ²⁶). Both *in vivo*
216 measurements and simulations had a duration of 12 minutes, with a temporal resolution of
217 16 seconds. Simulations were driven by a bi-exponential vascular input function, taken from
218 the literature.²⁷ Initially, 1% of the entire dose of the input function was partitioned across
219 all tumor inlets, weighted by the inflow rate for the individual inlet.

220 REANIMATE intravascular and interstitial Gd-DTPA delivery predictions were rendered as
221 videos (see **Supplementary Video 1** and **Supplementary Video 2**). Virtual sections from an
222 LS174T tumor are also shown in **Figure 5a**, which revealed a prolonged, peripheral
223 enhancement pattern, which is typical of the tumor type²⁰. In **Figure 5b** we show plots of
224 contrast agent uptake, in which the greyscale coloring of each curve represents distance
225 from the tumor edge (darkest at the edge, lightest in the centre). These reveal a highly

226 heterogeneous enhancement pattern, with decreasing concentration for increasing
227 proximity to the tumor centre. Conversely, we found that SW1222 tumors enhanced with
228 Gd-DTPA much more rapidly and homogeneously, with a peak enhancement at around 4
229 minutes, followed by a washout phase (see **Supplementary Figure 2**).

230 REANIMATE solutions describing Gd-DTPA delivery were analysed in the same manner as
231 experimental data, i.e. as a function of distance from the tumor periphery. Simulations were
232 performed in two stages: the first estimated Gd-DTPA enhancement using the initialisation
233 parameter values defined above (the naïve solution); the second stage used modified
234 parameter values, based on iteratively minimising the disparity between simulated and *in*
235 *vivo* data.

236 Our naïve analysis underestimated the magnitude of contrast enhancement in LS174T
237 tumors, but still reflected their spatial heterogeneity, with the S_0 parameter decreasing with
238 distance from the tumor periphery. The enhancement rate parameter, r_1 , provided a good fit
239 to *in vivo* data, but did not reflect its increasing value at the tumor centre. To account for
240 this, we increased the mean vascular permeability to $0.9 \times 10^{-6} \text{ cm s}^{-1}$ at the periphery, with a
241 linear increase to $1.1 \times 10^{-6} \text{ cm s}^{-1}$ in the centre, which provided a better accordance with *in*
242 *vivo* data (see **Supplementary Figure 3**). For the SW1222 tumor naïve simulation, contrast
243 agent uptake was overestimated, but homogeneously distributed, reflecting what was found
244 *in vivo*. The rate of enhancement was also much greater than *in vivo*. We therefore
245 uniformly decreased vascular permeability to $0.75 \times 10^{-7} \text{ cm s}^{-1}$ in the second simulation,
246 which then provided a good accordance with *in vivo* data ($p < 0.01$, Kolmogorov-Smirnov).
247 Scatter plots of the data, shown in **Supplementary Figure 1d**, also revealed a significant
248 correlation ($r^2 = 0.92$, $p < 0.001$, Pearson).

249 We can therefore conclude from these experiments that REANIMATE can provide good
250 estimates of the delivery of Gd-DTPA, but which can be further improved by *in vivo*
251 measurements.

252 *Dual-fluorophore optical imaging of response to Oxi4503 treatment*

253 Using our optimised Gd-DTPA delivery data, we went on to investigate the ability of
254 REANIMATE to model drug uptake and response to treatment. This required the
255 development of a dual-fluorophore imaging technique that allowed measurements of tumor
256 vascular structure at two separate time points to be encoded. We chose to model vascular
257 targeting therapy, due to its rapid, well-characterised mechanism of action, which can be

258 captured with *in vivo* MRI²⁸. The acute effects of VDAs have been well-documented, using
259 histology,^{29,30} MRI³¹ and *in vivo* confocal microscopy,³² which have demonstrated rapid
260 vascular shutdown and extensive vessel fragmentation within the first 60 minutes to 24
261 hours of administration. This causes decreased perfusion, especially in the central part of
262 the tumor,^{31,33} and an associated increase in hypoxia and cell death.³³ In this study, we
263 investigated a single dose of Oxi4503, at 40 mg kg⁻¹.

264 Our dual-fluorophore method allowed us to characterise blood vessel structure at two
265 separate time points, by administering fluorescently-labelled lectin (AlexaFluor-568) just
266 prior to injecting Oxi4503, and then a second lectin 90 minutes later (AlexaFluor-647). Our
267 rationale was that vessels occluded by Oxi4503, and were no longer perfused, would be
268 labelled by only the first fluorophore; vessels that remained perfused following therapy
269 would be labelled with both fluorophores. As a validation of our results, *in vivo* arterial spin
270 labelling (ASL) MRI was also performed on a subset of tumors (n=3 of each tumor type).
271 Mice, each bearing an LS174T or SW1222 tumor, were randomly assigned to treatment
272 (Oxi4503, 40 mg kg⁻¹) or control groups (administered saline). **Figure 6a** shows example
273 volume renderings of dual-stained vessel networks, in which vessels were colored *blue* if co-
274 labelled with both fluorescent lectins (i.e. vessels that were perfused both pre- and at 90
275 minutes post-Oxi4503 administration) or *green* if perfusion was evident pre-treatment but
276 had been removed at 90 minutes. See **Supplementary Video 3** for a three-dimensional
277 rendering of the data.

278 **Figures 6b to 6d** document the effect of Oxi4503 on the geometry of LS174T and SW1222
279 vessel networks. **Figure 6b** shows a graph comparing the mean distance of blood vessels
280 from the centre of each tumor type, pre- and post-treatment with Oxi4503. This plot shows
281 that, for LS174T tumors, vessel that became non-perfused with Oxi4503 (i.e. vessels
282 rendered in green) were generally located in the centre of tumors, whereas SW1222
283 displayed a more distributed and localised pattern of perfusion loss. In **Figure 6c** we show a
284 plot of the number of graphical nodes within each cluster that became isolated by this loss
285 of perfusion, which was significantly different between LS174T and SW1222 tumors
286 (LS174Ts displayed much larger clusters (P<0.01)). This further demonstrates the
287 fragmented nature of the SW1222 tumors' response to Oxi4503.

288 To ensure that these changes in vascular geometry were induced by the action of Oxi4503,
289 blood volume was measured pre- and post-Oxi4503 and compared against control groups
290 that received saline only. As can be seen in **Figure 6d**, Oxi4503 induced a significant decrease

291 in both tumor types ($P < 0.01$), but in control tumors, no significant change was found
292 ($p > 0.05$).

293 *REANIMATE simulations of response to Oxi4503*

294 Having identified significant differences between SW1222 and LS174T tumors in their
295 vascular structural response to Oxi4503, we next aimed to use REANIMATE to simulate
296 changes in tumor perfusion and IFP induced by Oxi4503, to attempt to further explore these
297 differences. **Figures 7a-c** show the results of REANIMATE simulations of vascular flow, IFP
298 and interstitial perfusion in an example LS174T tumor, pre- and post-Oxi4503. Each reveals a
299 spatially heterogeneous response to the drug, with both increases and decreases in
300 perfusion and IFP observed within the same tumors, representing a redistribution of flow in
301 response to localised vascular occlusion.

302 These trends were replicated in *in vivo* ASL data (example images are shown in **Figure 7d**)
303 which measured a significant decrease in median tumor perfusion of 9.8% (from 0.61 to 0.55
304 $\text{mL min}^{-1} \text{g}^{-1}$, $p < 0.05$) in LS174T tumors, but which was accompanied by a significant *increase*
305 in the 90th percentile perfusion value (from 2.48 to 2.64 $\text{mL min}^{-1} \text{g}^{-1}$, $P < 0.01$). Our
306 REANIMATE simulations also predicted a decrease in IFP of 4.5 mm Hg, but accompanied by
307 an increase of 3.6 mm Hg in the 90th percentile. These results demonstrate a complex
308 redistribution of flow caused by the vascular disrupting agent at this early time point, which
309 we sought to better understand. In SW1222 tumors, *in vivo* measurements of perfusion and
310 IFP did not significantly change. Moreover, the fragmented nature of dual-labelled
311 fluorescence images meant that post-Oxi4503 steady-state simulations could not be
312 performed in SW1222 tumors.

313 Our first REANIMATE computational experiment aimed to simulate the uptake of Oxi4503,
314 using a similar approach as taken for Gd-DTPA uptake simulations, but over a longer
315 duration (90 minutes, with a temporal resolution of 10 seconds). Oxi4503 has a molar mass
316 of 332.35 g mol^{-1} (approximately one third that of Gd-DTPA), so, using the Stoke-Einstein
317 relation, D was set at $7.37 \times 10^{-5} \text{ mm}^2 \text{ s}^{-1}$. Systemic pharmacokinetics for Oxi4503 were taken
318 from the literature,³⁴ and expressed as an exponential decay function (Equ. 15). Both
319 intravascular and interstitial drug concentrations were simulated, and results are shown in
320 **Figure 8a** (see, **Supplementary Video 4** for a four-dimensional representation). As with Gd-
321 DTPA experiments, Oxi4503 uptake was spatially heterogeneous.

322 We then used these REANIMATE simulations of Oxi4503 uptake to test two hypotheses: 1)
323 that vessels that receive the greatest Oxi4503 exposure are more likely to become non-
324 perfused; 2) that network geometry differences between tumor types could influence their
325 response to VDA therapy.

326 To test the first hypothesis, we compared vessels from our dual-labelled datasets that had
327 lost perfusion post-Oxi4503 (i.e. were labelled with just one fluorophore), with their
328 simulated exposure to Oxi4503, as predicted by REANIMATE. The box graph in **Figure 8b**
329 displays the result of this analysis, in which nodes connecting only non-perfused ('green')
330 vessels had a significantly lower exposure to Oxi4503 than nodes connecting a mixture of
331 non-perfused and perfused ('blue') vessels ($P < 0.05$). Similarly, **Figure 8c** and **8d** show the
332 location of perfused and non-perfused vessels and the cumulative exposure to Oxi4503 at 90
333 minutes post-administration, which shows non-perfused regions with low Oxi4503
334 exposure; on average non-perfused vessels exhibited a significantly lower simulated
335 exposure than vessels that remained perfused (2.0 compared with 3.8 mM min m^{-2}
336 ($p < 0.001$)). These results are inconsistent with our first hypothesis, that perfusion loss would
337 be associated with greater Oxi4503 exposure, and so the hypothesis was rejected. This lead
338 us to next evaluate our second hypothesis, and investigate differences in the vascular
339 architecture of the two tumor types. In particular, we evaluated the functional connectivity
340 of the two tumor types.

341 Functional (or logical) connectivity and redundancy measures describe the connectedness of
342 individual vessel networks, following pathways of decreasing fluid pressure. Specifically,
343 redundancy was measured by N , the mean number of viable alternative pathways for each
344 node if the shortest path (based on flow velocity) were occluded, and r , the average
345 additional distance that would be travelled. Connectivity was defined as the sum of the
346 number of nodes upstream and the number of nodes downstream of a given node, divided
347 by the total number of nodes in the network.

348 **Figures 9a** and **b** show histograms comparing $\log(C)$ and r measurements in LS174T and
349 SW1222 tumors. These data revealed that SW1222 tumors had significantly greater vascular
350 connectivity than LS174T tumors ($C = 0.15 \pm 0.06$ and 0.06 ± 0.05 , respectively) ($P < 0.01$).
351 They also display greater redundancy, with $N = 1.9 \pm 0.9$ and 1.5 ± 0.7 and $r = 1.02 \pm 0.02$ and
352 1.04 ± 0.05 , for SW1222 and LS174T tumors, respectively. Regional connectivity was also
353 mapped, with examples shown in **Figures 9c** (LS174T tumor) and **d** (SW1222 tumor), in
354 which nodes are scaled and color-coded according to their connectivity measure. These

355 clearly show the greater connectivity evident in this example SW1222 tumor, than in the
356 LS174T tumor.

357 Referring back to the definitions of connectivity and redundancy above, these results
358 suggest that, in LS174T tumors, vessels that become non-perfused due to targeting by a high
359 concentration of Oxi4503 can cause large vascular territories downstream to become non-
360 perfused, due to their lack of connectivity. In SW1222 tumors, loss of perfusion can be
361 compensated for by rerouting flow through alternative routes, thanks to their high
362 redundancy. This explanation, which requires further evaluation, would explain the
363 different pattern of response observed in SW1222 and LS174T tumors, with LS174T tumors
364 showing large regions of perfusion loss in dual-fluorophore data (particularly in their core),
365 whilst SW1222 show a more distributed pattern with flow loss in individual vessels.

366 **Discussion**

367 Computational modelling of cancer has a relatively long history,³⁵⁻³⁹ and has provided
368 valuable improvements in our understanding of the development and treatment of cancer.
369 As noted by Altrock, Liu and Michor, “the power of mathematical modelling lies in its ability
370 to reveal previously unknown or counterintuitive physical principles that might have been
371 overlooked or missed by a qualitative approach to biology”.³⁹ Successes have been found in
372 a range of areas, from modelling the dynamics of mutation acquisition⁴⁰ to multiscale
373 modelling of the interaction between tumor cells and their microenvironment.⁴¹ Previous,
374 seminal studies have combined experimental and numerical approaches to study the
375 relationship between tumor microstructure and the delivery of therapeutic agents.^{36,37,42} A
376 key observation from this work was that the chaotic organisation of tumor blood vessels,
377 their highly permeable vessel walls and missing or non-functioning lymphatics can result in
378 elevated interstitial fluid pressure (IFP) and limited blood flow. Both of these effects,
379 alongside high cell density and thick extracellular matrix, can conspire to limit the delivery of
380 systemically administered therapeutic agents, and can therefore act as a source of
381 therapeutic resistance.⁴³

382 Whilst these principles are well established, the complex manner in which these phenomena
383 can interact and vary within real-world tumors, and how individual drugs of different sizes
384 and physico-chemical properties are distributed, is not well understood. This points to a
385 critical need for better understanding of drug delivery to solid tumors, which could, at least
386 in part, help to address the pharmaceutical industry’s current low approval rate for new

387 cancer therapies, for which the influence of delivery is often an overlooked factor^{44,45}.
388 Equally, this knowledge could provide improvements in the clinical management of the wide
389 range of tumor types encountered in the clinic and enable treatments to be more effectively
390 personalised. This is an example of an area in which we believe our REANIMATE framework
391 will find wide application.

392 In this study, we introduced and provided a first demonstration of the application of
393 REANIMATE, which is a large-scale, three-dimensional imaging, modelling and analysis
394 framework, which uses data from optical imaging of cleared tissue^{16,46,47} to produce realistic
395 substrates for computational modelling of fluid dynamics in the tumor microenvironment,
396 optionally guided by *in vivo* imaging data. We applied REANIMATE to imaging data from
397 murine models of colorectal cancer and glioma to simulate: 1) steady-state fluid dynamics
398 (blood flow, intravascular and interstitial fluid pressure); 2) uptake of the MRI contrast agent
399 Gd-DTPA; and 3) uptake and response to vascular-targeting treatment (Oxi4503). Our results
400 demonstrated the feasibility and accuracy of this whole-tissue approach to numerical
401 modelling, which allows computational experiments to be performed on real-world tumors.
402 A key advantage of this approach is the ability to directly compare modelling solutions with
403 experimental measurements from the same tumors.

404 Whilst, in principle, any number of physiological phenomena could be incorporated into the
405 REANIMATE framework, we have initially focussed on modelling intravascular and interstitial
406 delivery. This used well-established biophysical models, but on a larger scale than has
407 previously been undertaken, and using real-world vascular networks. A justification for
408 simulations at this scale is provided by the multi-scale interactions evident in tumor fluid
409 dynamics. For example, elevated IFP is maintained via a whole-tumor distribution of both
410 vascular perfusion and interstitial drainage; likewise, perfusion is spatially heterogeneous,
411 meaning that one tumor sub-region can be very different to another.

412 Previous studies have used mathematical modelling approaches to study tumor blood and
413 interstitial flow, and have often focussed on their associated spatial heterogeneity.⁴⁸ For
414 example, Baxter and Jain^{36,42} described raised, homogeneous interstitial fluid pressure at
415 the centre of tumors, which drops precipitously at the tumor periphery. This result was
416 based, in part, on simulations of spherical, spatially-homogeneous tumor vasculature.
417 Numerous studies have subsequently incorporated more realistic vasculature into models
418 stemming from Baxter and Jain's work, such as synthetically-generated vascular networks,⁴⁹⁻
419 ⁵³ using micro-CT data from microvascular casts to model intravascular blood flow,⁵⁴ or using

420 subnetworks from tumors, derived from imaging data.⁵⁵⁻⁵⁷ Synthetically-generated
421 vasculature, using angiogenesis models, have been used to formulate hypotheses on the
422 delivery of chemotherapeutics^{58,59}, investigate the impact of tumor size on
423 chemotherapeutic efficacy⁶⁰ and to investigate the effect of dynamic vasculature⁶¹ and the
424 structure and morphology of vascular networks⁶² on drug delivery.

425 REANIMATE builds on and extends this work by including simulation substrates from
426 complete, real-world tumors, in three spatial dimensions, which are guided by and
427 compared against *in vivo* measurements. In this initial demonstration, we focussed on the
428 vasculature of colorectal xenograft models, which we imaged by labelling with fluorescent
429 lectin, allowing blood and interstitial flow to be explicitly simulated in realistic networks. We
430 treated the interstitium as a continuum, but future generations of the framework could
431 include additional structural elements such as cell membranes and nuclei, by
432 multifuorescence labelling. Indeed, there is significant potential for extending and
433 enhancing REANIMATE in other pathologies, to allow more in-depth computational
434 experiments to be performed.

435 A key advantage of REANIMATE is its ability to compare model predictions with
436 experimental measurements from the same tumors. We found a good correspondence
437 between our predictions of vascular perfusion and delivery of Gd-DTPA, and those from *in*
438 *vivo* imaging, both in their magnitude and spatial distribution. Perfusion was predicted to be
439 significantly greater in SW1222 tumors than in LS174T tumors, which reflects the results of *in*
440 *vivo* arterial spin labelling measurements, and was highly heterogenous, with flow
441 concentrated at the periphery of both tumor types. Conversely, Gd-DTPA uptake was more
442 heterogeneous in LS174T than SW1222 tumors, both in *in vivo* MRI measurements and
443 simulations (with minimal parameter optimisation).

444 Through its use of real-world, whole tumor substrates, REANIMATE undertakes modelling at
445 a whole-tissue scale. In many organs, this would enable pressure boundary conditions to be
446 defined in a straightforward manner, potentially by directly measuring inlet and outlet
447 pressures. However, subcutaneous tumor xenograft models normally exhibit a large number
448 of small feeding vessels, and so explicitly measuring and defining pressure boundary
449 conditions in this context is challenging. Our pressure boundary condition optimisation
450 procedure was a pragmatic solution to this problem, and enabled the use of target average
451 pressures. We found that the variability of pressure predictions (from which all other
452 parameters are ultimately derived), was much lower than the variability associated with

453 spatial heterogeneity within the tumor. However, this approach could still provide a source
454 of error and, whilst our model solutions agreed well with experimental measures, better
455 approaches could doubtless be developed. For example, as suggested above, the use of
456 tumors with a small number of well-defined inlet and outlet vessels, with measurable
457 pressures, would be advantageous, and the use of complete tumor vascular networks would
458 enable such an approach to be realised.

459 In summary, the results of this study show that, by adding realistic, whole-tumor
460 microstructure, with its inherent heterogeneity, accurate predictions for tumor fluid
461 dynamics and material delivery to be made. These results are important as Gd-DTPA can be
462 thought of as a proxy for delivery of a (non-metabolised) drug, enabling the accuracy of
463 REANIMATE delivery predictions to be verified. Indeed, REANIMATE could easily be modified
464 to include terms for metabolism, and acute response by the microenvironment could be
465 modelled by modifying cell density terms. This could therefore allow panels of drugs to be
466 assessed, with different delivery characteristics, to predict candidates that are most (or
467 least) likely to achieve a therapeutic response.

468 To further investigate this ability, we used REANIMATE to study the response of our
469 colorectal xenografts to Oxi4503 treatment, and showed that structural connectivity and
470 redundancy in colorectal tumor xenograft model vascular networks can introduce different
471 responses to the vascular-targeting agent Oxi4503. SW1222 tumors, with their greater
472 connectivity and redundancy, are more able to resist loss of flow in individual vessels, by
473 rerouting flow via local pathways, whereas there is much greater potential for LS174T
474 tumors to lose perfusion in large downstream subnetworks. These results reflect those that
475 we have previously observed *in vivo* when assessing the response of colorectal metastases
476 to Oxi4503 treatment in the liver,⁹ in which the magnitude of the response decreased with
477 increasing distance of individual tumors from major blood vessels. From a computational
478 modeling perspective, these results are also important, as they demonstrate a mechanism
479 through which tumors can become resistant to drug therapies, and which manifests via
480 complex interactions across large regions within a tumor, or across whole organs.

481 These results each demonstrate the important potential role for large, realistic tumor
482 simulations, of the form developed here with REANIMATE. The detailed insights generated
483 in this study could not have been made with conventional two-dimensional analysis of
484 histological sections, or *in vivo* experiments that lack the spatial resolution and functional
485 information to access this information, and demonstrates a key strength of the REANIMATE

486 approach. We anticipate that REANIMATE will enable us to further study and understand
487 complex interactions between biological phenomena, allowing new insights into key
488 challenges in cancer research. Whilst the limitations to drug delivery caused by the
489 physiological structuring of tumors have been well-studied,^{48,63} REANIMATE could enable a
490 better understanding of limitations in tumor drug delivery in individual tumors (and how this
491 can be mediated)^{36,64} and the development of resistance to therapy via physical (rather than
492 biochemical) mechanisms.⁶⁵ Moreover, if applied to biopsy samples, or resected, intact
493 tumors (or tumor deposits), could provide useful insights into treatment stratification in the
494 clinic.

495 **Acknowledgements**

496 We acknowledge the support received for the Kings College London & UCL CR-UK and EPSRC
497 Comprehensive Cancer Imaging Centre, in association with the MRC and Department of
498 Health (England), (C1519/A10331), Wellcome Trust (WT100247MA), Rosetrees Trust /
499 Stonegate Trust (M135-F1 and M601). We thank OXiGENE for supplying Oxi4503.

500 **Author Contributions**

501 Ad'E designed and performed optical imaging experiments, analysed and interpreted results
502 and wrote the first drafts of the manuscript. PS and RS developed software to perform
503 mathematical and computational analysis. PS analysed and interpreted data and wrote and
504 edited the paper. MA performed a subset of the optical imaging experiments. MS and SWS
505 developed software for performing time-dependent simulations. RR and TAR designed and
506 performed ASL-MRI measurements, and developed software for quantifying the data. GA
507 provided murine brain tumor models. AD assisted in student supervision and design of
508 optical imaging experiments. MFL provided access to imaging resources and student
509 supervision. RBP provided murine xenograft models and interpreted results. SWS developed
510 software for segmenting optical imaging data. RS and SWS secured funding, supervised the
511 design of experiments and simulations, developed the main concepts, interpreted results,
512 and contributed to the writing and editing of the manuscript.

513 **Competing Interests**

514 The authors declare no competing interests.

515 **Data availability**

516 Raw data generated from this study can be found at <http://doi.org/10.17605/OSF.IO/ZH9EU>

517 **Code availability**

518 Code used to analyse blood vessel networks in Python 2.7 is available in a GitHub repository,
519 and available under BSD licence: <https://github.com/CABI-SWS/reanimate>. Code used to
520 model tumor fluid dynamics in C++ is also available in a separate GitHub repository:
521 https://psweens.github.io/VF_NatureBioEng/

522 **Materials and Methods**

523 *Tumor xenograft models*

524 All experiments were performed in accordance with the UK Home Office Animals Scientific
525 Procedures Act 1986 and UK National Cancer Research Institute (NCRI) guidelines.⁶⁶ 8-10
526 week old, female, immune-compromised nu/nu nude mice (background CD1) were used
527 throughout this study (Charles River Laboratories). Human colorectal adenocarcinoma cell
528 lines (SW1222 and LS147T) were cultured in complete media (Minimum Essential Medium
529 Eagle with L-Glutamine (EMEM) (Lonza, Belgium) + 10% fetal bovine serum (Invitrogen, UK))
530 in a ratio 1:20 (v/v) and incubated at 37 °C and 5% CO₂. To prepare for injection, cells were
531 washed with DPBS and detached with trypsin-EDTA (7-8 min, 37 °C, 5% CO₂). A 100 µl bolus
532 of 5x10⁶ cells was injected subcutaneously into the right flank above the hind leg. Tumor
533 growth was measured daily with callipers, for between 10 to 14 days.

534 *Orthotopic glioma models*

535 Female, 8 week old, C57BL/6 mice were injected with 2x10⁴ GL261 mouse glioma cells. Mice
536 were anesthetized with 4% isoflurane in an induction box and then transferred to a
537 stereotactic frame (David Kopf Instrument, Tujunga, CA), where anaesthesia was delivered
538 through a nose cone and maintained at 2%. The head was sterilised with 4% chlorhexidine
539 and the skin was cut with a sterile scalpel to expose the skull. Coordinates were taken using
540 a blunt syringe (Hamilton, 75N, 26s/2"/3, 5 µL): 2mm right and 1mm anterior to the bregma,
541 corresponding to the right caudate nucleus. A burr hole was made using a 25-gauge needle.
542 The Hamilton syringe was lowered 4mm below the dura surface and then retracted by 1mm

543 to form a small reservoir. 2×10^4 GL261 cells were injected in a volume of 2 μ L over two
544 minutes. After leaving the needle in place for 2 minutes, it was retracted at 1 mm/min. The
545 burr hole was closed with bone wax (Aesculap, Braun) and the scalp wound was closed using
546 Vicryl Ethicon 6/0 suture.

547 *Fluorescent labelling of tumor vasculature and perfusion fixation*

548 Lectin (*griffonia simplicifolia*) bound to either Alexa-647 (Thermo Fisher Scientific, L32451) or
549 Alexa-568 (Thermo Fisher Scientific, L32458) was injected intravenously (i.v.) and allowed to
550 circulate for 5 minutes, prior to perfuse fixation, to allow sufficient binding to the vascular
551 endothelium.²

552 To prevent blood clot formation within the vasculature, mice were individually heparinized
553 by intraperitoneal (i.p.) injection (0.2 ml, with 1000 IU ml^{-1}). Mice were terminally
554 anaesthetized by i.p. injection of 100 mg kg^{-1} sodium pentobarbital (Animalcare, Pentोजect)
555 diluted in 0.1 ml phosphate buffered saline (PBS). Once anaesthesia was confirmed, surgical
556 procedures for intracardial perfusion were performed for systemic clearance of blood. PBS
557 (30 ml, maintained at 37 °C) was administered with a perfusion pump (Watson Marlow,
558 5058) at a flow rate of 3 ml/min to mimic normal blood flow. After the complete drainage of
559 blood, 40 ml of 4% paraformaldehyde (PFA, VWR chemicals) was administered. Harvested
560 tumors were stored for 12 hours in 4% PFA (10 ml total volume, at 4 °C).

561 *Treatment with Oxi4503*

562 Following 10 to 14 days of growth, mice were randomly assigned to treatment (Oxi4503,
563 $n=6$) and control (saline) groups, with $n=3$ SW122 and $n=3$ LS174T in each. Treated groups
564 were injected i.v. with 100 μ g lectin-AlexaFluor 647 diluted in sterile saline at neutral pH
565 (100 μ l) containing 1 mM CaCl_2 , followed by administration of OXi4503 (40 mg kg^{-1} , 4 mg ml^{-1}).
566 Control mice were injected with 100 μ l saline. After 2 hours, all mice were injected i.v.
567 with 100 μ g lectin-AlexaFluor 568 diluted in sterile saline at neutral pH (100 μ l) containing 1
568 mM CaCl_2 . 5 minutes after injection mice were culled and underwent perfuse-fixation, as
569 described above.

570 *Optical clearing and imaging*

571 Following perfuse-fixation, tumors were resected and rinsed three times in PBS, for 10
572 minutes each, prior to clearing, to remove residual formaldehyde and avoid over-fixation.⁶⁷
573 After PBS rinsing, harvested tumors were optically cleared with BABB (1:2 benzyl alcohol:

574 benzyl benzoate).⁶⁸ Our BABB clearing preparation consisted of dehydration in methanol for
575 48 hours followed by emersion in BABB for 48 hours.¹⁶

576 Fluorescently-labelled tumor vasculature in cleared tissue was visualized with optical
577 projection tomography (OPT, Bioptonics, MRC Technologies, Edinburgh). Lectin-AlexaFluor
578 647 was imaged using a filter set with excitation range 620/60 nm, and emission 700/75 nm.
579 For vessels labelled with lectin-AlexaFluor 568, a filter set with excitation 560/40 nm and
580 emission LP610 nm was used. Measurements were performed with an exposure time of
581 1600-2000 ms for lectin-AlexaFluor 647 and of 270-600 ms for lectin-AlexaFluor 568, which
582 was varied according to sample size. The rotation step was 0.45 degrees. The final resolution
583 ranged from 4.3 μm to 8 μm , depending on the sample size.⁶⁹

584 OPT data were reconstructed with Nrecon (Bruker, Ettlingen, Germany). Misalignment
585 compensation was used to correct misalignment during projection image acquisition, in
586 order to reduce tails, doubling or blurring in the reconstructed image. Depth of correction
587 for ring artefact reduction was 4 and defect pixel masking was 50% for all scans.

588 *Image processing and vessel segmentation*

589 Reconstructed OPT data were used to generate whole-tumor blood vessel networks. Firstly,
590 a three-dimensional Gaussian filter with a width of 50 pixels (corresponding to a physical
591 size of 300 μm , greater than the largest vessel diameter) was applied. The filtered data were
592 subtracted from the original data to remove background variations in autofluorescence. A
593 three-dimensional Frangi filter was then applied (Matlab, MathWorks, Natick, MA) to
594 enhance vessel-like structures.¹⁷ The response to the filter was thresholded to segment
595 blood vessels from background. Skeletonisation of these thresholded data was performed in
596 Amira (Thermo Fisher Scientific, Hillsboro, OR), which also converted the data into graph
597 format (i.e. nodes and segments with associated radii). To ensure that vessel structures
598 were accurately represented, 2D sections from the original image data were swept through
599 reconstructed 3D networks (in Amira), with visual inspection used to for an accordance
600 between vessel location and thickness, and the location of fluorescence signal.

601 *Mathematical model of steady-state tissue fluid dynamics*

602 Blood flow through the segmented vascular network was modelled by Poiseuille's law, using
603 empirically-derived laws for blood viscosity (assuming constant network haematocrit) and
604 following the established approach developed in ^{70,71} and applied to numerous tissues (for

605 example mesentery,^{72,73} muscle,⁷⁴ cortex,⁷⁵ and tumours^{54,76}). This model assumes
 606 conservation of flux at vessel junctions to define a linear system to solve for the pressures at
 607 nodal points in the network (from which vessel fluxes are calculated using Poiseuille).
 608 Boundary conditions on terminal nodes in the network were estimated using the
 609 optimisation method of Fry et al.,⁷³ which matches the network solution to target mean
 610 shear stress and pressure values.

611 The approach of Fry et al.⁷³ requires a proportion of boundary conditions to be applied to a
 612 microvascular network. However, neither flow or pressure measurements were obtained in
 613 individual vessels *in vivo* for our tumor networks. As such, an optimisation procedure was
 614 employed to induce a physiological pressure drop (55 to 15 mmHg for both LS147T and
 615 SW1222 simulations) across peritumoral boundary vessels in a network.⁷⁷ Consistent with
 616 previous studies,^{78,79} 33% of internal nodes were assigned zero flow with all remaining
 617 boundary nodes determined using the optimisation algorithm of Fry et al.⁷³. This procedure
 618 was repeated until simulations ensured physiologically realistic tissue perfusion when
 619 compared to that gathered *in vivo* using ASL MRI.

620 The network flow solution was coupled to an interstitial fluid transport model, adapting the
 621 approach taken in Secomb et al.⁸⁰ to model oxygen delivery to tissue. The interstitium is
 622 modelled as a porous medium using Darcy's law,

$$\mathbf{u} = -\kappa \nabla p, \quad [1]$$

623 subject to $p \rightarrow p_i$ as $|\mathbf{x}| \rightarrow \infty$. Here, \mathbf{u} is the volume-averaged interstitial blood velocity
 624 (IFV), p is the interstitial fluid pressure (IFP), p_i is the target IFP, and κ is the hydraulic
 625 conductivity of the interstitial tissue. Starling's law is used to describe fluid transport across
 626 the endothelium, from the vessels into the interstitium:

$$q = L_p S \cdot (\Delta p - \sigma \Delta \Pi), \quad [2]$$

627 where, q is the fluid flux across the endothelium, L_p is the hydraulic conductance of the
 628 vessel wall, S is the surface area of the vasculature, σ is the oncotic reflection coefficient
 629 and, Δp and $\Delta \Pi$ fluid and oncotic pressure gradients between the vasculature and tissue.

630 To solve the model computationally, we discretized the tumor vasculature into a series of M
 631 sources of strength $q_{s,j}$ so that the conservation of mass equation is modified to

$$-\kappa \nabla^2 p = \sum_{j=1}^M q_{s,j}(\mathbf{x}) \delta(\mathbf{x} - \mathbf{x}_j), \quad [3]$$

632 where \mathbf{x}_j and $q_{s,j}$ are the spatial coordinates and (unknown) strength at \mathbf{x}_j of source j ,

633 respectively, and $\delta(\mathbf{x}-\mathbf{x}_j)$ is the three-dimensional delta function. An axisymmetric Greens
 634 solution, $G(r)$ where $r=|\mathbf{x}-\mathbf{x}_j|$, was sought for equation 3 subject to the boundary condition
 635 that to $p \rightarrow p_I$ as $|\mathbf{x}| \rightarrow \infty$, motivated by distributing the delta function $\delta(\mathbf{x}-\mathbf{x}_j)$ uniformly
 636 over a sphere of finite radius r_{0j} (set to the radius of blood vessel j), the solution to equation
 637 3 may be approximated by

$$638 \quad G_{ij} = \begin{cases} 3 - \left(\frac{r_{ij}}{r_{0j}}\right)^2 \\ \frac{3 - \left(\frac{r_{ij}}{r_{0j}}\right)^2}{8\pi\kappa r_{0j}}, & r_{ij} \geq r_{0j} \\ \frac{1}{4\pi\kappa r_{ij}}, & r_{ij} < r_{0j} \end{cases} \quad [4]$$

639 where $r_{ij}=|\mathbf{x}_i-\mathbf{x}_j|$ is the distance between sources $i,j \in M$. The corresponding interstitial
 640 fluid pressure (IFP) at source i may be approximated by

$$p_i = p_I + \sum_{j=1}^N G_{ij}q_{s,j}, \quad \text{for } i \in M. \quad [5]$$

641 Assuming flux of fluid across the wall of vessel i , $q_{v,i}$, is continuous yields

$$q_{v,i} = -2\pi\kappa r_{v,i} l_i \sum_{j=1}^M \nabla G_{ij}q_{s,j}. \quad [6]$$

642 Starling's law, equation 2, can be written in the form

$$p_{v,i} = p_{b,i} - Kq_{v,i} - \sigma(\Pi_{b,i} - \Pi_{v,i}), \quad \text{for } i \in M, \quad [7]$$

643 where $p_{v,i}$ and $\Pi_{v,i}$ are the blood and oncotic pressure at the vessel wall, $p_{b,i}$ and $\Pi_{b,i}$ is the
 644 intravascular blood pressure in the absence of diffusive interstitial fluid transfer (calculated
 645 using the Poiseuille flow model) and oncotic pressure, and $q_{v,i}$ is the rate of fluid flow per
 646 unit volume from blood vessel i to the interstitium. The intravascular resistance to fluid
 647 transport, is defined by $K = 1/L_p S$.

648 Equations 5, 6 and 7 were combined to form a dense linear system, which was solved to give
 649 the IFP field throughout the tissue. Parameter values for the complete mathematical model
 650 are shown in **Supplementary Table 2**.

651 *Mathematical model of time-dependent vascular and interstitial transport*

652 A 'propagating front' (PF) algorithm was developed to describe the transport of solute (e.g. a
 653 drug) through the tumor vessel network and interstitium. This model considers the
 654 timescale for delivery of a drug, on which the flow problem is assumed to be steady (the
 655 timescales for drug transport by advection and diffusion are much faster than those for
 656 vascular adaption, which would contribute to a non-steady flow solution). A vascular input
 657 function was first defined, which describes the time-dependent delivery of the drug
 658 concentration into the network, and which then propagates throughout the network

659 according to the network topology and flow solution. The influence of each vessel network
 660 inlet was modelled independently and each solution linearly superimposed, allowing the
 661 algorithm to be parallelised.

662 Each node was assigned a set of values, J describing the ratio of the flow in each vessel
 663 segment connected to the node (F), to the total inflow into the node (F_{in}). Flow values were
 664 taken from the steady-state model defined above. The J values were propagated through
 665 the network, following pathways with decreasing vascular pressure. Using velocities from
 666 the steady-state solution, delays (d) were also assigned to each vessel segment. Vessel
 667 segments attached to each node were catergorised as outflows (negative pressure gradient)
 668 or inflows (positive pressure gradient). Time-dependent drug concentration in the k^{th}
 669 outflowing vessel segment ($C_k(t)$) was modelled as

$$C_k(t) = J_k \sum_{j=1}^N C_j(t - d_k), \quad [8]$$

670 where $C_j(t)$ is the concentration in the j^{th} inflowing vessel segment and N is the total number
 671 of inflowing vessel segments.

672 Interstitial delivery was cast in a forward finite difference framework, in which vessels were
 673 considered as radial emitters. Points were gridded on concentric cylinders, regularly spaced
 674 around the vessel segment (with spacing ranging from 10 to 100 μm). Exchange of the drug
 675 across the vessel wall and diffusion through the interstitium were modelled as

$$C_{j+1}^i(r) = AC_j^i(r) + \Gamma(C_j^v - C_j^i(r)), \quad [9]$$

$$C_{j+1}^v = \sum_{j=1}^N \Gamma(C_j^i - C_j^v), \quad [10]$$

676 where C_{j+1}^i is the interstitial concentration at the j^{th} time point (at a radial distance r from
 677 the vessel) and C_j^v is the vascular concentration. Interstitial velocity and pressure were not
 678 used in the time-dependent model, for simplicity, but could be incorporated in future
 679 studies, which could be particularly relevant for simulating the delivery of large molecules.
 680 The coefficient A is a two-dimensional square matrix of dimension n , where n is the number
 681 of radial positions in the interstitial finite difference calculation, h is their radial separation
 682 and k is the spacing between time steps:

$$A = \begin{bmatrix} 1 - 2\lambda & \lambda & 0 & 0 & 0 & 0 \\ \lambda & 1 - 2\lambda & \lambda & 0 & 0 & 0 \\ 0 & \lambda & 1 - 2\lambda & \lambda & 0 & 0 \\ \vdots & \vdots & \vdots & \vdots & \ddots & \vdots \\ 0 & 0 & 0 & 0 & \lambda & 1 - 2\lambda \end{bmatrix} \quad [11]$$

$$\lambda = \frac{Dk}{h^2} \quad [12]$$

683 Here D is the diffusion coefficient of the agent under investigation. Following each finite
684 difference step, interstitial diffusion solutions were regrided to a course $64 \times 64 \times 64$ matrix
685 (approximately $100 \mu\text{m}$ isotropic resolution) for storage. During regriding, molar quantities
686 were converted to molar concentration, with the parameter Γ controlling the transport
687 across the vessel wall,

$$\Gamma = \frac{L_p S}{V Q n} \quad [13]$$

688 in which, for small molecules, transport was assumed to be diffusive, and pressure terms
689 were assumed to be negligible.

690 *Measurement of vessel network functional connectivity and redundancy*

691 The mean number of viable alternative pathways, N , for each node if the shortest path
692 (based on transit time – i.e. incorporating flow velocity) was occluded was used to define the
693 redundancy of tumor vessel networks, alongside r , the average additional distance that
694 would be travelled.⁸¹ Connectivity was defined as the sum of the number of nodes upstream
695 and the number of nodes downstream of a given node, divided by the total number of nodes
696 in the network. All three measures reflect functional connectivity (i.e. following pathways
697 with decreasing vascular pressure from steady-state fluid dynamics simulations), and were
698 estimated from vessel networks using algorithms written in-house in Python 2.7.

699 *Simulation of Gd-DTPA delivery*

700 The systemic pharmacokinetics for Gd-DTPA in mice, following an i.v. bolus injection, were
701 modelled as a biexponential decay:

$$C^v(t) = a_1 e^{-m_1 t} + a_2 e^{-m_2 t} \quad [14]$$

702 with $a_1 = 2.55 \text{ mM}$, $m_1 = 8 \times 10^{-2} \text{ s}^{-1}$, $a_2 = 1.2 \text{ mM}$ and $m_2 = 1 \times 10^{-3} \text{ s}^{-1}$.²⁷

703 *Measurement of vessel network functional connectivity and redundancy*

704 The mean number of viable alternative pathways, N , for each node if the shortest path
705 (based on transit time – i.e. incorporating flow velocity) was occluded was used to define the
706 redundancy of tumor vessel networks, alongside r , the average additional distance that
707 would be travelled.⁸¹ Connectivity was defined as the sum of the number of nodes upstream
708 and the number of nodes downstream of a given node, divided by the total number of nodes
709 in the network. All three measures reflect functional connectivity (i.e. following pathways

710 with decreasing vascular pressure from steady-state fluid dynamics simulations), and were
711 estimated from vessel networks using algorithms written in-house in Python 2.7.

712 *Simulation of Gd-DTPA delivery*

713 The systemic pharmacokinetics for Gd-DTPA in mice, following an i.v. bolus injection, were
714 modelled as a biexponential decay:

$$C^v(t) = a_1 e^{-m_1 t} + a_2 e^{-m_2 t} \quad [14]$$

715 with $a_1 = 2.55 \text{ mM}$, $m_1 = 8 \times 10^{-2} \text{ s}^{-1}$, $a_2 = 1.2 \text{ mM}$ and $m_2 = 1 \times 10^{-3} \text{ s}^{-1}$.²⁷

716 *Simulation of Oxi4503 delivery*

717 Oxi4503 systemic pharmacokinetics were modelled as a single exponential function, of the
718 form

$$C^v(t) = C_{\max} e^{-R_{1/2} t} \quad [15]$$

719 with $R_{1/2} = 3.1 \times 10^{-5} \text{ s}^{-1}$ and $C_{\max} = 7.7 \text{ } \mu\text{M}$.³⁴ This assumed a mouse mass of 25 g and injection
720 dose of 40 mg kg^{-1} .

721 *Dynamic contrast-enhanced MRI*

722 Gadolinium-DTPA (Magnevist, Bayer, Leverkusen, Germany) was injected as a bolus into
723 mouse tail veins, using a power injector (Harvard Instruments, Cambourne, UK). We injected
724 5 mL kg^{-1} over a period of 5 seconds, which was initiated at 90 seconds after the start of a
725 dynamic, spoiled gradient-echo sequence (TE, 2.43 ms; TR, 15 ms; flip angle 20° ; 5 slices;
726 slice thickness 0.5 mm; matrix size, 128×128 ; FOV, $35 \times 35 \text{ mm}$; temporal resolution 16 s;
727 total duration 15 minutes). The change in signal intensity induced by contrast agent was
728 calculated by subtracting the mean signal from the first 5 frames from the acquisition.

729 Signal intensity was converted to gadolinium concentration, via the change in longitudinal
730 relaxation rate R_1 and contrast agent relaxivity (c_1 fixed at $2.9 \text{ mM}^{-1} \text{ s}^{-1}$):

$$C(t) = \frac{R_1(t) - R_{10}}{c_1} \quad [16]$$

731 $R_1(t)$ was estimated from the theoretical change in spoiled gradient-echo signal magnitude.⁸²

732 R_{10} was the mean, pre-enhancement R_1 , which was estimated from a Look-Locker multi-

733 inversion time acquisition,⁸³ acquired prior to the dynamic sequence (TE, 1.18 ms; inversion
734 time spacing, 110 ms; first inversion time, 2.3 ms; 50 inversion recovery readouts).

735 Contrast agent uptake data were fitted to a phenomenological model of the form

$$C(t) = S_0(1 - e^{-r_1(t-t_0)})e^{-r_2(t-t_0)} \quad [17]$$

736 where S_0 , r_1 , r_2 and t_0 were fitted parameters. Fitting was performed in Python 2.7 (leastq
737 algorithm from the scipy package).

738 *Arterial spin labelling MRI*

739 We acquired arterial spin labeling (ASL) data with a flow-sensitive alternating inversion
740 recovery (FAIR) Look-Locker ASL sequence, with a single-slice spoiled gradient echo readout
741 (echo time, 1.18 ms; inversion time spacing, 110 ms; first inversion time, 2.3 ms; 50
742 inversion recovery readouts; 4 averages).^{9,83} Regional perfusion maps were calculated as
743 described by Belle et al. (38), with an assumed blood-partition constant of 0.9.

744 *Statistics*

745 Differences between groups were tested for significance with the non-parametric, two-sided
746 Wilcoxon rank sum test (Python 2.7, scikit package). $P < 0.05$ was considered significant. All
747 summary data are presented as mean \pm SD.

748 **References**

- 749 1 Brocato, T. *et al.* Understanding Drug Resistance in Breast Cancer with
750 Mathematical Oncology. *Curr Breast Cancer Rep* **6**, 110-120,
751 doi:10.1007/s12609-014-0143-2 (2014).
- 752 2 Dobosz, M., Ntziachristos, V., Scheuer, W. & Strobel, S. Multispectral
753 fluorescence ultramicroscopy: three-dimensional visualization and
754 automatic quantification of tumor morphology, drug penetration, and
755 antiangiogenic treatment response. *Neoplasia (New York, N.Y)* **16**, 1-13
756 (2014).
- 757 3 Jahrling, N., Becker, K. & Dodt, H. U. 3D-reconstruction of blood vessels by
758 ultramicroscopy. *Organogenesis* **5**, 227-230 (2009).
- 759 4 Walls, J. R., Sled, J. G., Sharpe, J. & Henkelman, R. M. Resolution
760 improvement in emission optical projection tomography. *Physics in
761 medicine and biology* **52**, 2775-2790, doi:10.1088/0031-
762 9155/52/10/010 (2007).
- 763 5 Alizadeh, A. A. *et al.* Toward understanding and exploiting tumor
764 heterogeneity. *Nature medicine* **21**, 846-853, doi:10.1038/nm.3915
765 (2015).

- 766 6 Jain, R. K. Transport of molecules in the tumor interstitium: a review.
767 *Cancer research* **47**, 3039-3051 (1987).
- 768 7 Housman, G. *et al.* Drug resistance in cancer: an overview. *Cancers (Basel)*
769 **6**, 1769-1792, doi:10.3390/cancers6031769 (2014).
- 770 8 Gaya, A., Akle, C. A., Mudan, S. & Grange, J. The Concept of Hormesis in
771 Cancer Therapy - Is Less More? *Cureus* **7**, e261, doi:10.7759/cureus.261
772 (2015).
- 773 9 Johnson, S. P. *et al.* Acute changes in liver tumour perfusion measured
774 non-invasively with arterial spin labelling. *Br J Cancer* **114**, 897-904,
775 doi:10.1038/bjc.2016.51 (2016).
- 776 10 El Emir, E. *et al.* Predicting response to radioimmunotherapy from the
777 tumor microenvironment of colorectal carcinomas. *Cancer research* **67**,
778 11896-11905, doi:10.1158/0008-5472.CAN-07-2967 (2007).
- 779 11 Folarin, A. A., Konerding, M. A., Timonen, J., Nagl, S. & Pedley, R. B. Three-
780 dimensional analysis of tumour vascular corrosion casts using
781 stereoinaging and micro-computed tomography. *Microvascular research*
782 **80**, 89-98, doi:10.1016/j.mvr.2010.03.007 (2010).
- 783 12 Walker-Samuel, S. *et al.* In vivo imaging of glucose uptake and metabolism
784 in tumors. *Nature medicine* **19**, 1067-1072, doi:10.1038/nm.3252 (2013).
- 785 13 Rajkumar, V. S. *et al.* A comparative study of PDGFR inhibition with
786 imatinib on radiolabeled antibody targeting and clearance in two
787 pathologically distinct models of colon adenocarcinoma. *Tumour biology :*
788 *the journal of the International Society for Oncodevelopmental Biology and*
789 *Medicine* **33**, 2019-2029, doi:10.1007/s13277-012-0461-9 (2012).
- 790 14 El-Emir, E. *et al.* Characterisation and radioimmunotherapy of L19-SIP, an
791 anti-angiogenic antibody against the extra domain B of fibronectin, in
792 colorectal tumour models. *Br J Cancer* **96**, 1862-1870, doi:6603806 [pii]
793 10.1038/sj.bjc.6603806 (2007).
- 794 15 Lankester, K. J. *et al.* Combretastatin A-4-phosphate effectively increases
795 tumor retention of the therapeutic antibody, 131I-A5B7, even at doses
796 that are sub-optimal for vascular shut-down. *International journal of*
797 *oncology* **30**, 453-460 (2007).
- 798 16 d'Esposito, A., Nikitichev, D., Desjardins, A., Walker-Samuel, S. & Lythgoe,
799 M. F. Quantification of light attenuation in optically cleared mouse brains.
800 *Journal of biomedical optics* **20**, 80503, doi:10.1117/1.JBO.20.8.080503
801 (2015).
- 802 17 Frangi, A. F., Niessen, W. J., Vincken, K. L. & Viergever, M. A. in *Medical*
803 *Image Computing and Computer-Assisted Intervention — MICCAI'98*. (eds
804 Wells W.M., Colchester A., & Delp S.) (Springer, Berlin, Heidelberg).
- 805 18 Thomas, D. L., Lythgoe, M. F., Pell, G. S., Calamante, F. & Ordidge, R. J. The
806 measurement of diffusion and perfusion in biological systems using
807 magnetic resonance imaging. *Physics in medicine and biology* **45**, R97-138
808 (2000).
- 809 19 Konerding, M. A. *et al.* Evidence for characteristic vascular patterns in
810 solid tumours: quantitative studies using corrosion casts. *Br J Cancer* **80**,
811 724-732, doi:10.1038/sj.bjc.6690416 (1999).
- 812 20 Walker-Samuel, S. *et al.* Investigating low-velocity fluid flow in tumours
813 using convection-MRI. *bioRxiv*, doi:10.1101/200279 (2017).

- 814 21 Walker-Samuel, S. *et al.* Investigating Low-Velocity Fluid Flow in Tumors
815 with Convection-MRI. *Cancer research* **78**, 1859-1872, doi:10.1158/0008-
816 5472.CAN-17-1546 (2018).
- 817 22 Yuan, F. *et al.* Vascular permeability in a human tumor xenograft:
818 molecular size dependence and cutoff size. *Cancer research* **55**, 3752-
819 3756 (1995).
- 820 23 Reyes-Aldasoro, C. C. *et al.* Estimation of apparent tumor vascular
821 permeability from multiphoton fluorescence microscopic images of P22
822 rat sarcomas in vivo. *Microcirculation* **15**, 65-79,
823 doi:10.1080/10739680701436350 (2008).
- 824 24 Panagiotaki, E. *et al.* Noninvasive quantification of solid tumor
825 microstructure using VERDICT MRI. *Cancer research* **74**, 1902-1912,
826 doi:10.1158/0008-5472.can-13-2511 (2014).
- 827 25 Tofts, P. S. Modeling tracer kinetics in dynamic Gd-DTPA MR imaging. *J*
828 *Magn Reson Imaging* **7**, 91-101 (1997).
- 829 26 Koh, T. S. *et al.* In vivo measurement of gadolinium diffusivity by dynamic
830 contrast-enhanced MRI: a preclinical study of human xenografts. *Magn*
831 *Reson Med* **69**, 269-276, doi:10.1002/mrm.24246 (2013).
- 832 27 Benjaminsen, I. C., Graff, B. A., Brurberg, K. G. & Rofstad, E. K. Assessment
833 of tumor blood perfusion by high-resolution dynamic contrast-enhanced
834 MRI: a preclinical study of human melanoma xenografts. *Magn Reson Med*
835 **52**, 269-276, doi:10.1002/mrm.20149 (2004).
- 836 28 Sheng, Y. *et al.* Combretastatin family member OXI4503 induces tumor
837 vascular collapse through the induction of endothelial apoptosis.
838 *International journal of cancer* **111**, 604-610, doi:10.1002/ijc.20297
839 (2004).
- 840 29 Chan, L. S., Malcontenti-Wilson, C., Muralidharan, V. & Christophi, C.
841 Alterations in vascular architecture and permeability following OXi4503
842 treatment. *Anti-Cancer Drugs* **19**, 17-22,
843 doi:10.1097/CAD.0b013e3282f077a1 (2008).
- 844 30 Salmon, H. W., Mladinich, C. & Siemann, D. W. Evaluations of vascular
845 disrupting agents CA4P and OXi4503 in renal cell carcinoma (Caki-1)
846 using a silicon based microvascular casting technique. *European Journal of*
847 *Cancer* **42**, 3073-3078, doi:<http://dx.doi.org/10.1016/j.ejca.2006.06.016>
848 (2006).
- 849 31 Salmon, H. W. & Siemann, D. W. Effect of the second-generation vascular
850 disrupting agent OXi4503 on tumor vascularity. *Clinical cancer research :
851 an official journal of the American Association for Cancer Research* **12**,
852 4090-4094, doi:10.1158/1078-0432.ccr-06-0163 (2006).
- 853 32 Wankhede, M., Dedeugd, C., Siemann, D. W. & Sorg, B. S. In vivo functional
854 differences in microvascular response of 4T1 and Caki-1 tumors after
855 treatment with OXi4503. *Oncology reports* **23**, 685-692 (2010).
- 856 33 El-Emir, E. *et al.* Tumour parameters affected by combretastatin A-4
857 phosphate therapy in a human colorectal xenograft model in nude mice.
858 *European journal of cancer (Oxford, England : 1990)* **41**, 799-806,
859 doi:10.1016/j.ejca.2005.01.001 (2005).
- 860 34 Kirwan, I. G. *et al.* Comparative preclinical pharmacokinetic and metabolic
861 studies of the combretastatin prodrugs combretastatin A4 phosphate and
862 A1 phosphate. *Clin Cancer Res* **10**, 1446-1453 (2004).

- 863 35 Byrne, H. M., Alarcon, T., Owen, M. R., Webb, S. D. & Maini, P. K. Modelling
864 aspects of cancer dynamics: a review. *Philos Trans A Math Phys Eng Sci*
865 **364**, 1563-1578, doi:10.1098/rsta.2006.1786 (2006).
- 866 36 Baxter, L. T. & Jain, R. K. Transport of fluid and macromolecules in tumors.
867 I. Role of interstitial pressure and convection. *Microvascular research* **37**,
868 77-104 (1989).
- 869 37 Baxter, L. T. & Jain, R. K. Transport of fluid and macromolecules in tumors.
870 II. Role of heterogeneous perfusion and lymphatics. *Microvascular*
871 *research* **40**, 246-263 (1990).
- 872 38 Baxter, L. T. & Jain, R. K. Transport of fluid and macromolecules in tumors.
873 III. Role of binding and metabolism. *Microvascular research* **41**, 5-23
874 (1991).
- 875 39 Altrock, P. M., Liu, L. L. & Michor, F. The mathematics of cancer:
876 integrating quantitative models. *Nat Rev Cancer* **15**, 730-745,
877 doi:10.1038/nrc4029 (2015).
- 878 40 Beerenwinkel, N., Schwarz, R. F., Gerstung, M. & Markowetz, F. Cancer
879 evolution: mathematical models and computational inference. *Syst Biol*
880 **64**, e1-25, doi:10.1093/sysbio/syu081 (2015).
- 881 41 Masoudi-Nejad, A. *et al.* Cancer systems biology and modeling:
882 microscopic scale and multiscale approaches. *Semin Cancer Biol* **30**, 60-
883 69, doi:10.1016/j.semcancer.2014.03.003 (2015).
- 884 42 Boucher, Y., Baxter, L. T. & Jain, R. K. Interstitial pressure gradients in
885 tissue-isolated and subcutaneous tumors: implications for therapy.
886 *Cancer research* **50**, 4478-4484 (1990).
- 887 43 Senthebane, D. A. *et al.* The Role of Tumor Microenvironment in
888 Chemoresistance: To Survive, Keep Your Enemies Closer. *Int J Mol Sci* **18**,
889 doi:10.3390/ijms18071586 (2017).
- 890 44 Rubin, E. H. & Gilliland, D. G. Drug development and clinical trials--the
891 path to an approved cancer drug. *Nature reviews. Clinical oncology* **9**, 215-
892 222, doi:10.1038/nrclinonc.2012.22 (2012).
- 893 45 Jain, R. K. & Stylianopoulos, T. Delivering nanomedicine to solid tumors.
894 *Nature Reviews Clinical Oncology* **7**, 653, doi:10.1038/nrclinonc.2010.139
895 (2010).
- 896 46 Renier, N. *et al.* iDISCO: a simple, rapid method to immunolabel large
897 tissue samples for volume imaging. *Cell* **159**, 896-910,
898 doi:10.1016/j.cell.2014.10.010 (2014).
- 899 47 Chung, K. *et al.* Structural and molecular interrogation of intact biological
900 systems. *Nature* **497**, 332-337, doi:10.1038/nature12107 (2013).
- 901 48 Jain, R. K., Martin, J. D. & Stylianopoulos, T. The role of mechanical forces
902 in tumor growth and therapy. *Annual review of biomedical engineering* **16**,
903 321-346, doi:10.1146/annurev-bioeng-071813-105259 (2014).
- 904 49 Soltani, M. & Chen, P. Numerical Modeling of Interstitial Fluid Flow
905 Coupled with Blood Flow through a Remodeled Solid Tumor
906 Microvascular Network. *PLoS One* **8**, e67025,
907 doi:10.1371/journal.pone.0067025 (2013).
- 908 50 Sefidgar, M. *et al.* Numerical modeling of drug delivery in a dynamic solid
909 tumor microvasculature. *Microvascular research* **99**, 43-56,
910 doi:10.1016/j.mvr.2015.02.007 (2015).

- 911 51 Mohammadi, M. & Chen, P. Effect of microvascular distribution and its
912 density on interstitial fluid pressure in solid tumors: A computational
913 model. *Microvascular research* **101**, 26-32,
914 doi:10.1016/j.mvr.2015.06.001 (2015).
- 915 52 Zhao, J., Salmon, H. & Sarntinoranont, M. Effect of heterogeneous
916 vasculature on interstitial transport within a solid tumor. *Microvascular*
917 *research* **73**, 224-236 (2007).
- 918 53 Baish, J. W. *et al.* Role of Tumor Vascular Architecture in Nutrient and
919 Drug Delivery: An Invasion Percolation-Based Network Model.
920 *Microvascular research* **51**, 327-346,
921 doi:<https://doi.org/10.1006/mvre.1996.0031> (1996).
- 922 54 Stamatelos, S. K., Kim, E., Pathak, A. P. & Popel, A. S. A bioimage
923 informatics based reconstruction of breast tumor microvasculature with
924 computational blood flow predictions. *Microvascular research* **91**, 8-21,
925 doi:10.1016/j.mvr.2013.12.003 (2014).
- 926 55 Boujelben, A. *et al.* Multimodality imaging and mathematical modelling of
927 drug delivery to glioblastomas. *Interface Focus* **6**, 20160039,
928 doi:10.1098/rsfs.2016.0039 (2016).
- 929 56 Thurber, G. M. *et al.* Single-cell and subcellular pharmacokinetic imaging
930 allows insight into drug action in vivo. *Nature communications* **4**, 1504,
931 doi:10.1038/ncomms2506
932 <https://www.nature.com/articles/ncomms2506#supplementary-information>
933 (2013).
- 934 57 van de Ven, A. L. *et al.* Integrated intravital microscopy and mathematical
935 modeling to optimize nanotherapeutics delivery to tumors. *AIP Advances*
936 **2**, 011208, doi:10.1063/1.3699060 (2012).
- 937 58 Stéphanou, A., McDougall, S. R., Anderson, A. R. A. & Chaplain, M. A. J.
938 Mathematical modelling of flow in 2D and 3D vascular networks:
939 Applications to anti-angiogenic and chemotherapeutic drug strategies.
940 *Mathematical and Computer Modelling* **41**, 1137-1156,
941 doi:<https://doi.org/10.1016/j.mcm.2005.05.008> (2005).
- 942 59 Sinek, J. P. *et al.* Predicting drug pharmacokinetics and effect in
943 vascularized tumors using computer simulation. *Journal of Mathematical*
944 *Biology* **58**, 485, doi:10.1007/s00285-008-0214-y (2008).
- 945 60 Steuperaert, M. *et al.* Mathematical modeling of intraperitoneal drug
946 delivery: simulation of drug distribution in a single tumor nodule. *Drug*
947 *Delivery* **24**, 491-501, doi:10.1080/10717544.2016.1269848 (2017).
- 948 61 Sefidgar, M. *et al.* Numerical modeling of drug delivery in a dynamic solid
949 tumor microvasculature. *Microvascular research* **99**, 43-56,
950 doi:<https://doi.org/10.1016/j.mvr.2015.02.007> (2015).
- 951 62 McDougall, S. R., Anderson, A. R. A., Chaplain, M. A. J. & Sherratt, J. A.
952 Mathematical modelling of flow through vascular networks: Implications
953 for tumour-induced angiogenesis and chemotherapy strategies. *Bulletin of*
954 *Mathematical Biology* **64**, 673-702, doi:10.1006/bulm.2002.0293 (2002).
- 955 63 Mitchell, M. J., Jain, R. K. & Langer, R. Engineering and physical sciences in
956 oncology: challenges and opportunities. *Nat Rev Cancer* **17**, 659-675,
957 doi:10.1038/nrc.2017.83 (2017).

- 958 64 Baronzio, G., Parmar, G. & Baronzio, M. Overview of Methods for
959 Overcoming Hindrance to Drug Delivery to Tumors, with Special
960 Attention to Tumor Interstitial Fluid. *Front Oncol* **5**, 165,
961 doi:10.3389/fonc.2015.00165 (2015).
- 962 65 Olive, K. P. *et al.* Inhibition of Hedgehog signaling enhances delivery of
963 chemotherapy in a mouse model of pancreatic cancer. *Science (New York,*
964 *N.Y)* **324**, 1457-1461, doi:10.1126/science.1171362 (2009).
- 965 66 Workman, P. *et al.* Guidelines for the welfare and use of animals in cancer
966 research. *Br J Cancer* **102**, 1555-1577 (2010).
- 967 67 Janssen, F. J. A study of the absorption and scattering factors of light in
968 whole blood. *Medical & biological engineering* **10**, 231-240 (1972).
- 969 68 Dodt, H. U. *et al.* Ultramicroscopy: three-dimensional visualization of
970 neuronal networks in the whole mouse brain. *Nature methods* **4**, 331-336,
971 doi:10.1038/nmeth1036 (2007).
- 972 69 Jonkman, J. E., Swoger, J., Kress, H., Rohrbach, A. & Stelzer, E. H. Resolution
973 in optical microscopy. *Methods in enzymology* **360**, 416-446 (2003).
- 974 70 Pries, A. R. *et al.* Resistance to blood flow in microvessels in vivo. *Circ Res*
975 **75**, 904-915 (1994).
- 976 71 Pries, A. R., Secomb, T. W. & Gaehtgens, P. The endothelial surface layer.
977 *Pflugers Archiv : European journal of physiology* **440**, 653-666,
978 doi:10.1007/s004240000307 (2000).
- 979 72 Pries, A. R. & Secomb, T. W. Microvascular blood viscosity in vivo and the
980 endothelial surface layer. *Am J Physiol Heart Circ Physiol* **289**, H2657-
981 2664, doi:10.1152/ajpheart.00297.2005 (2005).
- 982 73 Fry, B. C., Lee, J., Smith, N. P. & Secomb, T. W. Estimation of blood flow
983 rates in large microvascular networks. *Microcirculation* **19**, 530-538,
984 doi:10.1111/j.1549-8719.2012.00184.x (2012).
- 985 74 Fry, B. C., Roy, T. K. & Secomb, T. W. Capillary recruitment in a theoretical
986 model for blood flow regulation in heterogeneous microvessel networks.
987 *Physiol Rep* **1**, e00050, doi:10.1002/phy2.50 (2013).
- 988 75 Sweeney, P. W., Walker-Samuel, S. & Shipley, R. J. Insights into cerebral
989 haemodynamics and oxygenation utilising in vivo mural cell imaging and
990 mathematical modelling. *Sci Rep* **8**, 1373, doi:10.1038/s41598-017-
991 19086-z (2018).
- 992 76 Pries, A. R. *et al.* Structural adaptation and heterogeneity of normal and
993 tumor microvascular networks. *PLoS computational biology* **5**, e1000394,
994 doi:10.1371/journal.pcbi.1000394 (2009).
- 995 77 Sweeney, P. W., Walker-Samuel, S. & Shipley, R. J. Modelling the transport
996 of fluid through heterogeneous, real-world tumour substrates. (2017).
- 997 78 Morikawa, S. *et al.* Abnormalities in pericytes on blood vessels and
998 endothelial sprouts in tumors. *Am J Pathol* **160**, 985-1000,
999 doi:10.1016/S0002-9440(10)64920-6 (2002).
- 1000 79 Stamatelos, S. K., Androulakis, I. P., Kong, A. N. & Georgopoulos, P. G. A
1001 semi-mechanistic integrated toxicokinetic-toxicodynamic (TK/TD) model
1002 for arsenic(III) in hepatocytes. *J Theor Biol* **317**, 244-256,
1003 doi:10.1016/j.jtbi.2012.09.019 (2013).
- 1004 80 Secomb, T. W., Hsu, R., Park, E. Y. & Dewhirst, M. W. Green's function
1005 methods for analysis of oxygen delivery to tissue by microvascular
1006 networks. *Ann Biomed Eng* **32**, 1519-1529 (2004).

- 1007 81 Xu, X., Chen, A., Jansuwan, S., Heaslip, K. & Yang, C. Modeling
1008 Transportation Network Redundancy. *Transportation Research Procedia*
1009 **9**, 283-302, doi:10.1016/j.trpro.2015.07.016 (2015).
- 1010 82 Schabel, M. C. & Parker, D. L. Uncertainty and bias in contrast
1011 concentration measurements using spoiled gradient echo pulse
1012 sequences. *Physics in medicine and biology* **53**, 2345-2373,
1013 doi:10.1088/0031-9155/53/9/010 (2008).
- 1014 83 Ramasawmy, R. *et al.* Hepatic arterial spin labelling MRI: an initial
1015 evaluation in mice. *NMR Biomed* **28**, 272-280, doi:10.1002/nbm.3251
1016 (2015).
- 1017
- 1018

1019 **Figure Captions**

1020 **Figure 1.** The REANIMATE pipeline for *in vivo* and *ex vivo* imaging of intact tumors and
1021 performing three-dimensional computational fluid mechanics simulations. After *in vivo*
1022 imaging (1), which can be performed longitudinally during tumor growth, tumors are
1023 resected and optically cleared (2), to render tumors transparent for three-dimensional
1024 fluorescence imaging. Optical images are processed to segment fluorescently-labelled
1025 structures within the tumor microenvironment (3) (in this case, blood vessel networks),
1026 which are reconstructed in 3D graph format (nodes and connecting segments, each with a
1027 radius corresponding to the size of the blood vessel). These geometrical data become the
1028 substrate for computational fluid dynamic models to estimate steady-state blood flow and
1029 interstitial transport (4) and time-dependent numerical modelling of drug delivery (5). All of
1030 these data can then be used to perform *in silico* experiments (e.g. assessing the
1031 heterogeneous delivery of drugs or contrast agents), which can be compared with *in vivo*
1032 experiments in the same tumor models, or even the same mice. In this study, REANIMATE is
1033 used to study the action of a vascular disrupting agent (Oxi4503) in two models of human
1034 colorectal carcinoma.

1035 **Figure 2.** Three-dimensional blood vessel networks, segmented from optical imaging data
1036 acquired from complete colorectal carcinoma xenografts, and reconstructed in graphical
1037 format (diameters scaled according to their measured values). a) and b) show reconstructed
1038 networks from LS174T and SW1222 tumors, respectively, with inset panels showing
1039 zoomed-in regions. The two tumor types displayed significant differences in vascular
1040 architecture, as well as intra-tumor spatial heterogeneity. c) and d) show example LS174T
1041 vessel networks overlaid on raw image data. A good accordance can be seen between
1042 hyper-intense vessel structures in the image data and graphical format vessels.

1043 **Figure 3.** REANIMATE, steady-state simulation results example LS174T (a-e) and SW1222 (f-j)
1044 colorectal adenocarcinoma xenografts. (a, f) Three-dimensional visualisations of whole-
1045 tumor blood vessel networks, colored according to vessel radius, blood flow and
1046 intravascular pressure. (b, g) Three-dimensional rendering of REANIMATE interstitial fluid
1047 pressure predictions, in the same tumor as in (a, f), overlaid on the blood vessel network
1048 (grey). (c, h) Example *in vivo* measurements of tumor perfusion, acquired in a single slice
1049 through the tumor, using arterial spin labelling MRI (left) and the REANIMATE predicted
1050 perfusion from a single slice (with vessel structures overlaid in grey). Scatter plots comparing
1051 ASL measurements of perfusion and REANIMATE predictions are shown in **Supplementary**

1052 **Figures 1a** and **b**, respectively. (d, i) and (e, j) show REANIMATE predictions of interstitial
1053 fluid pressure and interstitial fluid velocity, respectively, in the same two-dimensional slice
1054 as in (c, h).

1055 **Figure 4.** REANIMATE simulations of steady-state fluid dynamics (vascular and interstitial) in
1056 an orthotopic murine glioma model (GL261). a) Segmented blood vessel networks, showing
1057 tumor vessels (red) and normal brain vessels (blue). The tumor was connected to the brain
1058 via several large feeding vessels at the interface between the two tissues. b) The results of
1059 REANIMATE vascular simulations, with vessel network color-coded for vessel radius, vascular
1060 pressure and blood flow. c) A three-dimensional rendering of REANIMATE interstitial fluid
1061 pressure predictions, with blood vessel network overlaid. d) Comparison of *in vivo*
1062 perfusion measurements with ASL-MRI and REANIMATE predictions. A scatter plot
1063 comparing ASL measurements of perfusion and REANIMATE predictions is shown in
1064 **Supplementary Figure 1c**. A complete slice through the brain is shown for ASL-MRI, with the
1065 tumor outlined with a black, dashed line. REANIMATE perfusion predictions show a slice
1066 through the tumor. (e) and (f) show REANIMATE predictions for interstitial fluid pressure
1067 and interstitial fluid velocity, respectively.

1068 **Figure 5.** REANIMATE simulation of Gd-DTPA (an MRI contrast agent) delivery to an example
1069 LS174T tumor, compared with uptake measured *in vivo* with DCE-MRI. (a) Gd-DTPA
1070 enhancement in a slice through the tumor, measured/simulated over 13 minutes. (b) Mean
1071 Gd-DTPA concentration as a function of time, for REANIMATE (left) and *in vivo* data (right).
1072 Each curve shows the average uptake at a fractional distance between the perimeter and
1073 centre of mass of the tumor. (c) Plot of a line profile through the tumor, at 13 minutes,
1074 corresponding to the black lines shown in (a). (d) A histogram of Gd-DTPA concentrations at
1075 13 minutes (also shown as a scatter plot in **Supplementary Figure 1d**).

1076 **Figure 6.** Dual-fluorophore, optical imaging of the response of colorectal carcinoma models
1077 (LS174T and SW1222) to treatment with a vascular disrupting agent (Oxi4503), at baseline
1078 and 90 minutes post-dosing. Tumors were injected with lectin labelled with the first
1079 fluorophore (AlexaFluor-568) prior to administration of 40 mg kg⁻¹ of Oxi4503, to label all
1080 blood vessels in the tumors. 60 minutes later, to assess the acute and heterogeneous effects
1081 of Oxi4503, a second lectin labelled with a different fluorophore (AlexaFluor-647) was
1082 injected, to label vessels that remained perfused. (a) Whole-tumor blood vessel networks,
1083 colored according to whether they remained labelled following Oxi4503 (dual-labelled, blue)
1084 or were no longer perfused (single-labelled, green). OPT signal intensity images are also

1085 shown. (b) Box plot showing the distance of single- and dual-labelled vessels from the tumor
1086 periphery and (c) the size of single-labelled clusters in both tumor types. (a-c) show that
1087 LS174T tumors lost large vascular regions at their centre, whereas SW1222 tumors showed a
1088 more distributed pattern of perfusion loss, distributed throughout the tumor. (d) Box plot of
1089 blood volume measurements from dual-labelled Oxi4503 and control-treated tumors. Blood
1090 volume significantly reduced ($p=0.0002$, two-sided Wilcoxon rank sum) in both SW1222 and
1091 LS174T tumors when treated with Oxi4503, whereas there was no significant difference in
1092 control tumors. In box plots, bar-ends define the range of the data, box-ends the inter-
1093 quartile range, and central bars are median values; asterisks denote statistically significant
1094 differences ($p<0.01$, two-sided Wilcoxon rank sum).

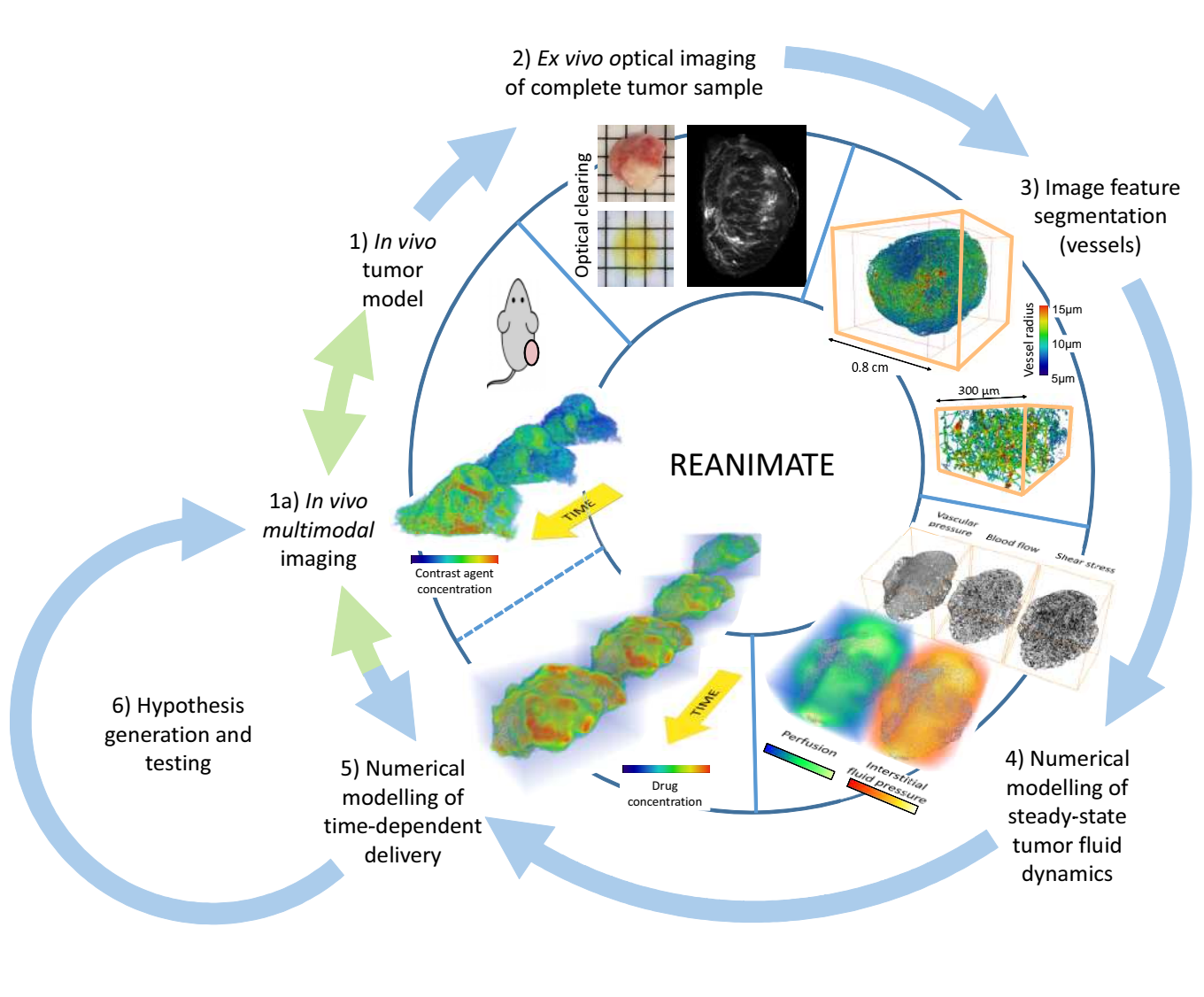
1095 **Figure 7.** Results of REANIMATE simulations of blood flow, perfusion and interstitial fluid
1096 pressure (IFP), in an LS174T tumor, at baseline (top row) and 90 minutes post-Oxi4503
1097 treatment (middle row). Images showing the change in perfusion *in vivo*, measured with
1098 arterial spin labelling MRI, are also shown, alongside histograms of each parameter (bottom
1099 row). Small changes in each parameter were observed, which were heterogeneously
1100 distributed throughout the tumor, both in simulations and *in vivo*.

1101 **Figure 8.** REANIMATE simulation predictions of Oxi4503 delivery and treatment response. (a)
1102 Maps of whole-tumor intravascular and interstitial (tissue) delivery of Oxi4503 from baseline
1103 to 90 minutes post-dosing. (b) Box plot of simulated Oxi4503 exposure in branch points
1104 connecting single-labelled only, dual-labelled only or a mixture of single- and dual-labelled
1105 vessels at 90 minutes post-Oxi4503 delivery. A significantly lower exposure to Oxi4503 was
1106 found in in single-labelled vessels, as denoted by an asterisk ($p=0.004$, two-sided Wilcoxon
1107 rank sum). Bar-ends define the range of the data, box-ends the inter-quartile range, and
1108 central bars are median values. (c-f) A 1 mm-thick slice through an LS174T vessel network,
1109 showing (c) the location of dual- and single-labelled vessel segments, (d) simulated Oxi4503
1110 exposure (intravascular and interstitial), (e) intravascular distance from an inlet node and (f)
1111 their connectivity score. Yellow arrows show the location of examples of single-label
1112 clusters, which are associated with a larger intravascular distance from an inlet, lower node
1113 connectivity and mixed (both high and intermediate) Oxi4503 exposure.

1114 **Figure 9.** Connectivity analysis of whole-tumor blood vessel networks. Frequency
1115 distributions of a) $\ln(C)$ (node connectivity) and b) redundancy distance ratio, r ,
1116 demonstrating clear distinctions in the distributions for the two colorectal carcinoma
1117 xenograft models (SW1222 and LS174T). c,d) Tumor blood vessel networks, with nodes

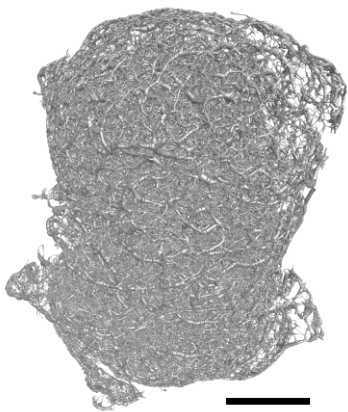
1118 scaled according to vessel connectivity; the larger the node, the greater the connectivity, for
1119 an LS174T tumor (c) and SW1222 tumor (d).

1120

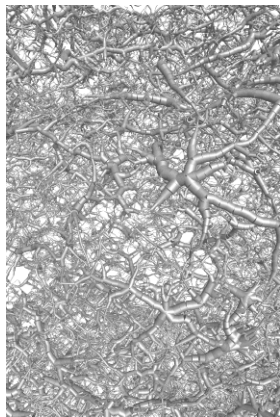


SW1222

a



0.25 cm



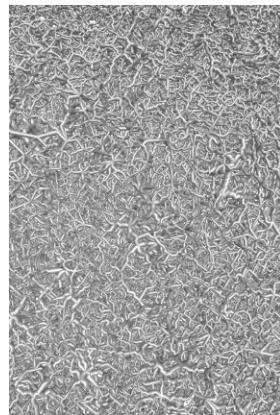
250 μ m

LS174T

b

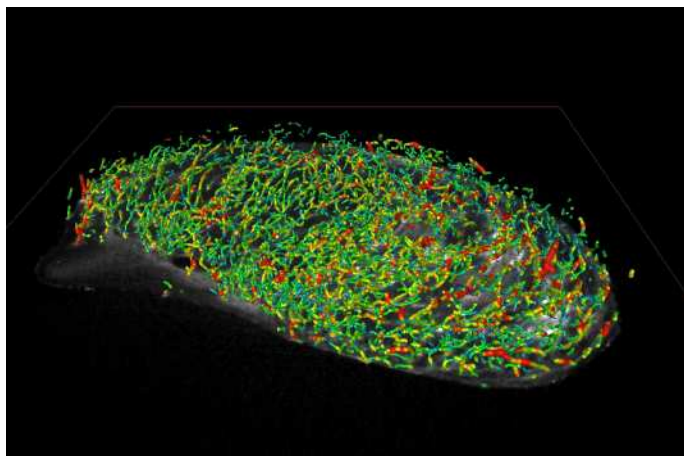
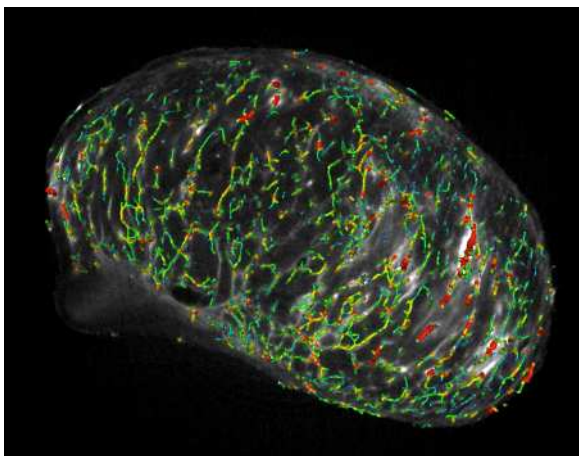


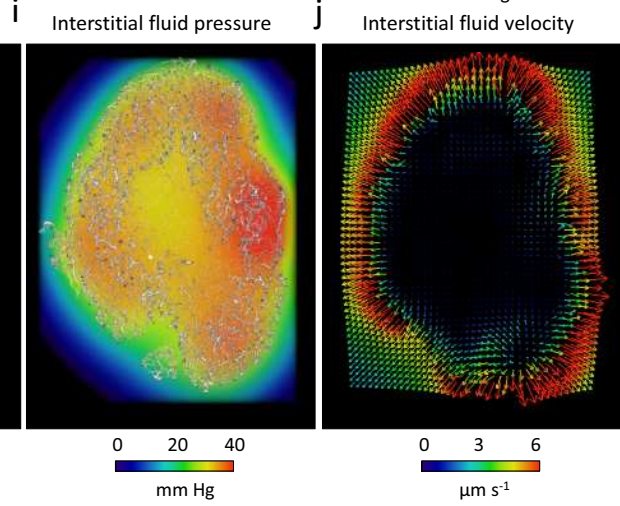
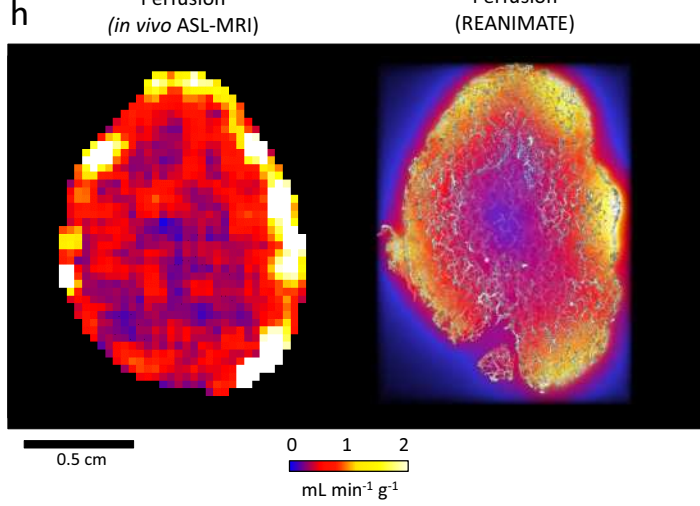
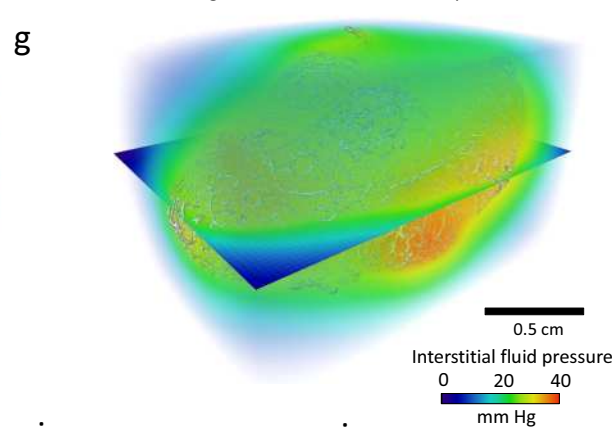
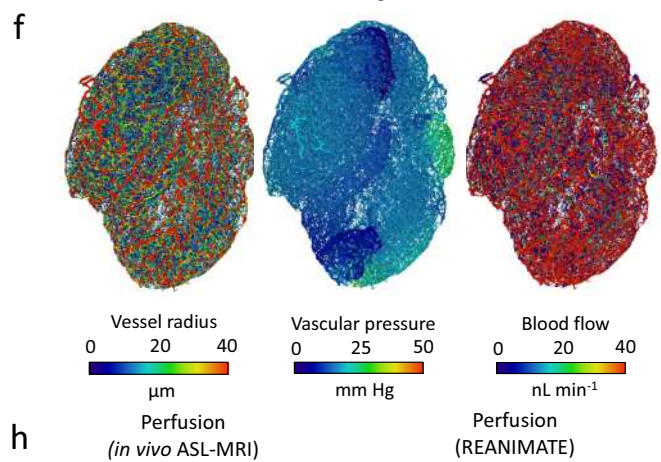
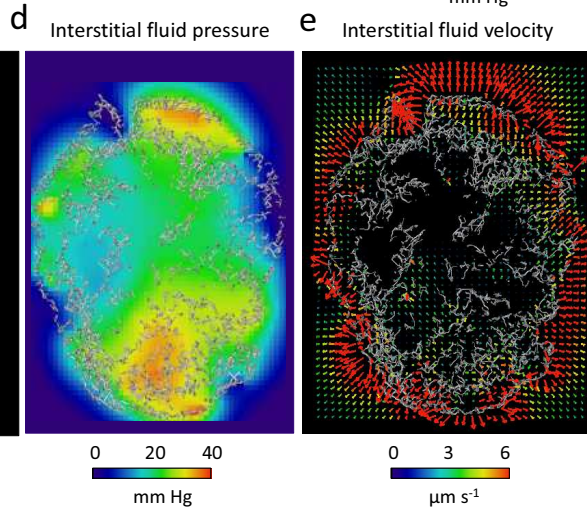
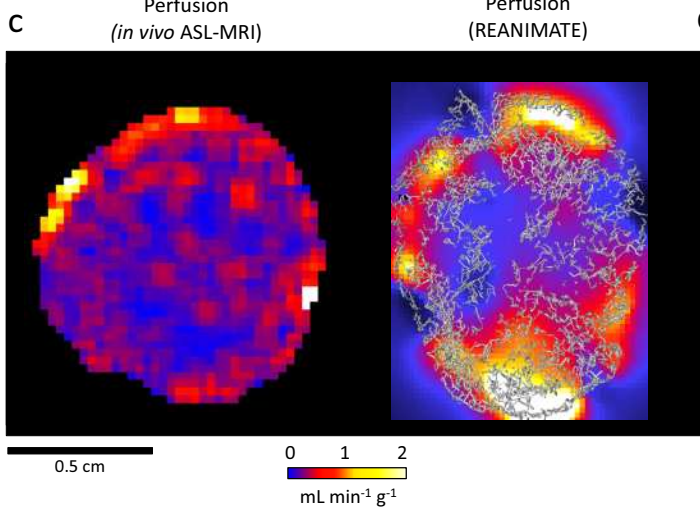
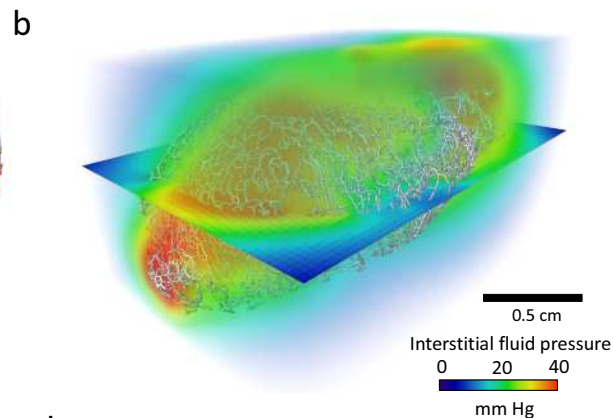
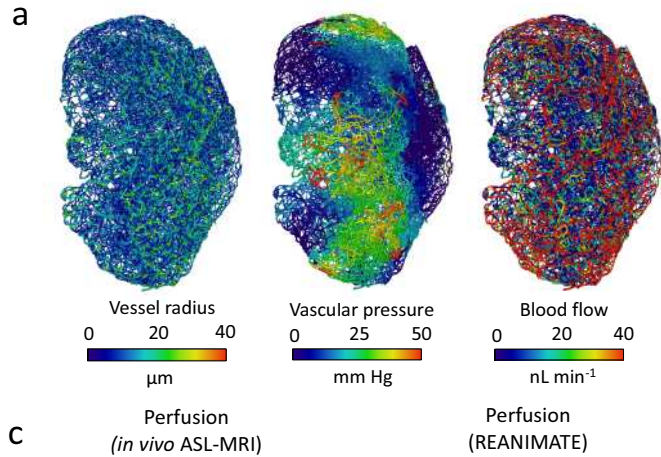
0.25 cm

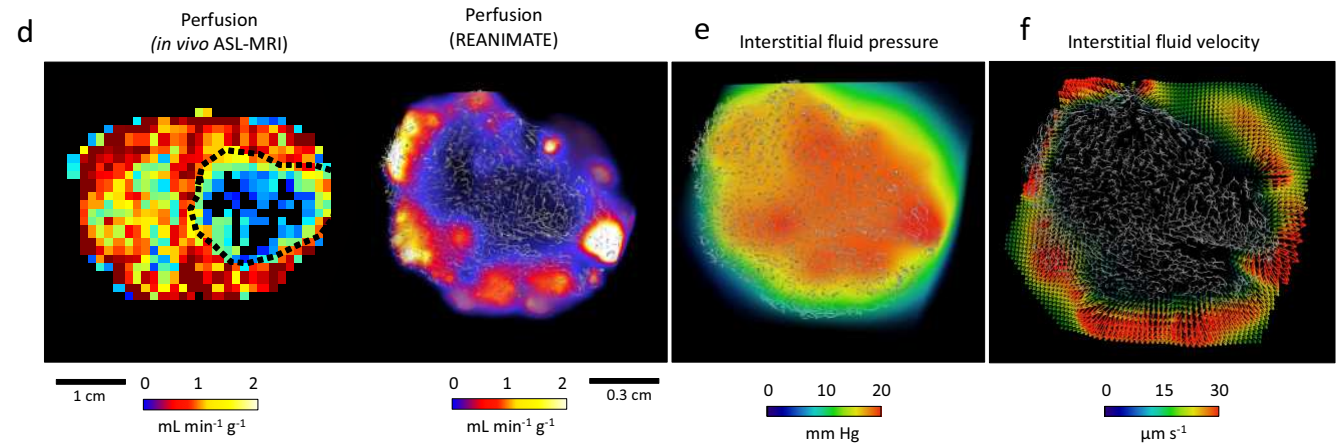
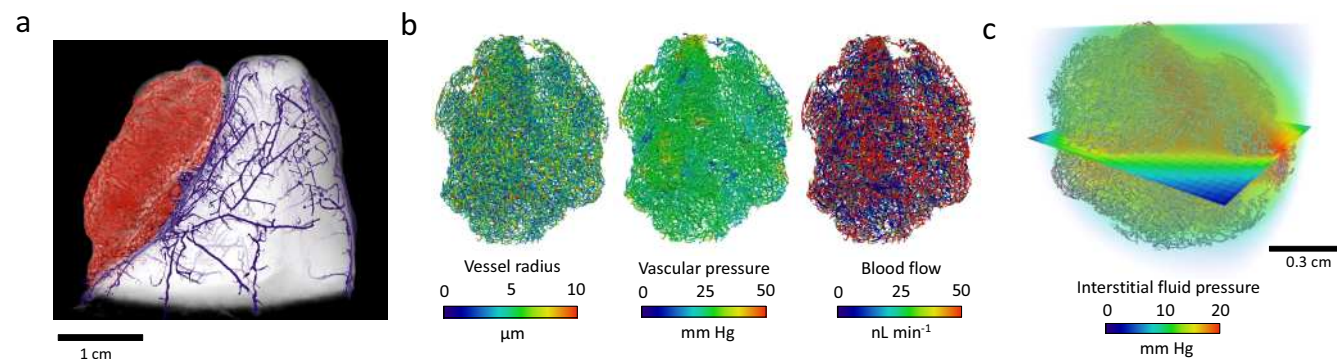


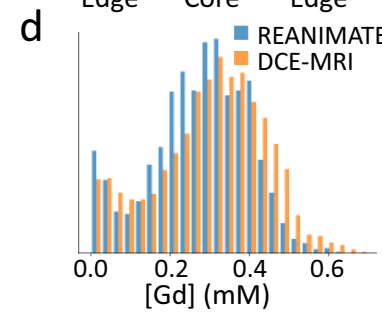
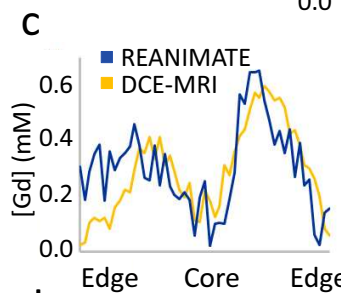
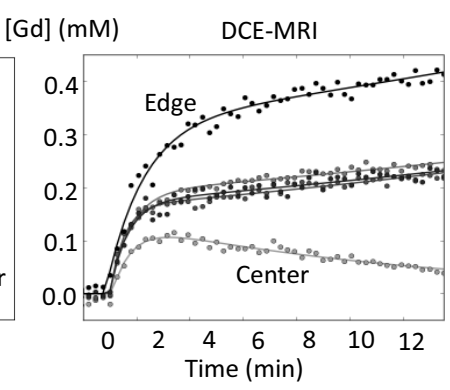
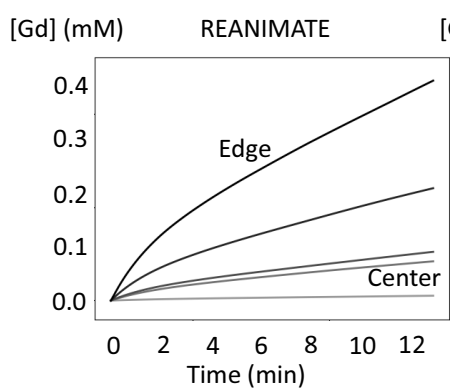
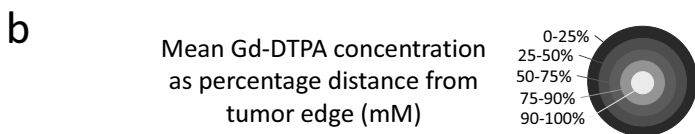
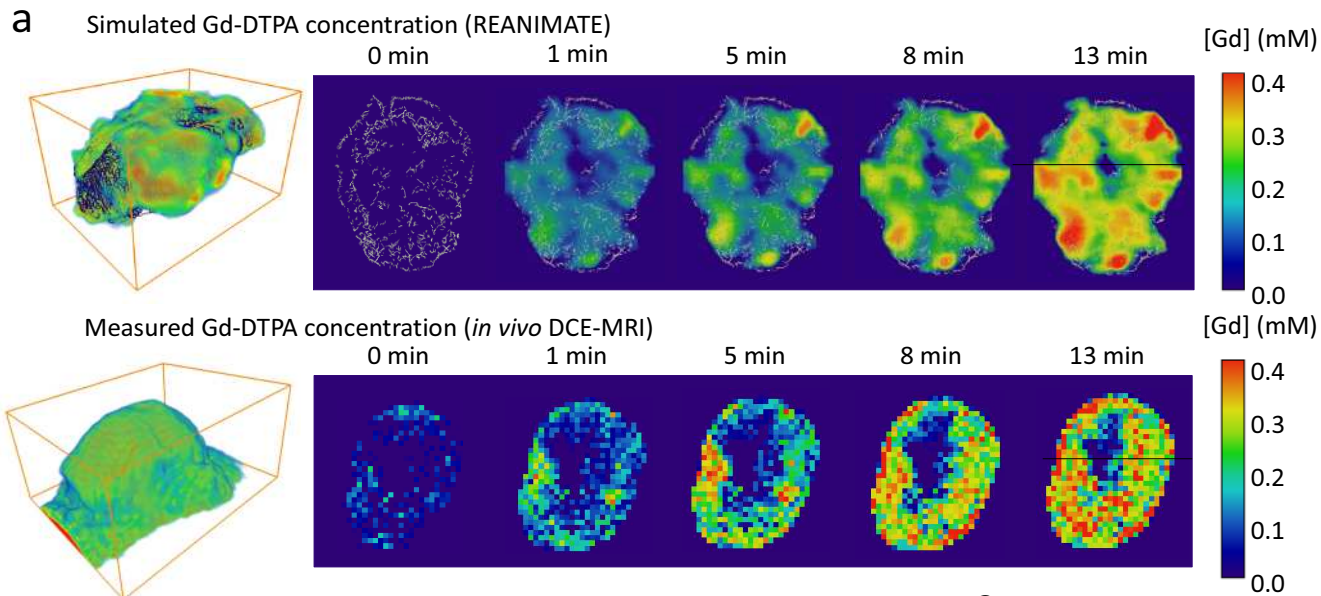
250 μ m

c









a

■ Vessels labelled at baseline only
■ Vessels labelled at baseline and at 90 minutes

